The Gluon Polarization in the Nucleon

from the COMPASS Experiment

Habilitationsschrift
zur
Erlangung der venia legendi
der
Mathematisch-Naturwissenschaftlichen Fakultät
der
Rheinischen Friedrich-Wilhelms-Universität Bonn

vorgelegt von
Jörg Pretz

Bonn, im April 2007

updated version June 2007

Abstract

This work describes the analysis and the results of the COMPASS collaboration on the measurement of the gluon polarization $\Delta G/G$ in the nucleon.

Inclusive polarized deep inelastic scattering experiments revealed that the spin or helicity contribution of quarks to the nucleon spin is surprisingly small. Typically values of $\Delta\Sigma = 20-30\%$ are found in contrast to much larger values of approximately 75% predicted by quark models. In principle quarks and gluons can contribute with their spin and orbital angular momentum to the nucleon spin of 1/2. This leads to the intuitive sum rule

$$\frac{1}{2} = \frac{1}{2}\Delta\Sigma + \Delta G + L_q + L_g \ ,$$

where $\Delta\Sigma$ is the contribution of the spin of the quarks, ΔG the contribution of the spin of the gluons, L_q and L_g the respective contributions of the quark and gluon orbital angular momentum.

Next-to-leading order (NLO) QCD analyses of inclusive data point to one possible solution to this so called spin puzzle: A large helicity contribution of the gluons $\Delta G = \int_0^1 \Delta G(x)\mathrm{dx}$ would lead to values of $\Delta\Sigma$ compatible with the values found in quark models. This is one of the motivations to measure ΔG.

Experimentally this quantity is accessible via the measurement of double spin asymmetries in two different processes: The first one is open charm production which provides the cleanest and most direct measurement. The second method is the production of hadron pairs with large transverse momentum. It has a higher statistical accuracy but is affected by a larger model dependence. In this work special emphasis is put on the analysis of the open charm data where a new method is developed to simultaneously determine signal and background asymmetries.

COMPASS results indicate that the helicity contribution of the gluons to the nucleon spin is small at a gluon momentum fraction $x_g \approx 0.1$. This is confirmed by other experiments and NLO analyses of inclusive data. Large values of ΔG of 2-3 are basically ruled out.

Contents

1 Introduction **3**

2 Deep Inelastic Scattering **5**

2.1 Kinematics of Deep Inelastic scattering 5
2.2 Deep Inelastic Scattering and the Quark Parton Model 9
2.3 Polarization Effects in Deep Inelastic Scattering 11
2.4 QCD corrections 13

3 The Nucleon Spin Puzzle **15**

3.1 The Static Quark Model 15
3.2 Relativistic Quark Models 16
3.3 Baryon Decays 16
3.4 Deep Inelastic Scattering 18
3.5 NLO Analysis of Deep Inelastic Scattering 19
  3.5.1 Determination of ΔG from NLO QCD analysis 19
3.6 Summary 21

4 How to measure ΔG? **22**

4.1 Open Charm Method 22
4.2 High p_T Method 23
4.3 Comparison of the two methods 24
  4.3.1 Gluon momentum fraction x_g 25
4.4 Other ways to measure ΔG 27

5 The COMPASS Experiment **29**

5.1 History 29
5.2 Beam 30
5.3 Polarized Target 30

5.4 Spectrometer 32
5.5 Trigger System 33

6 Analysis & Results **40**
6.1 Open Charm Analysis 40
6.1.1 Event Selection 40
6.1.2 Determination of $\Delta G/G$ 41
6.2 High p_T analysis 55
6.2.1 High p_T, $Q^2 < 1$ GeV^2 55
6.2.2 High p_T, $Q^2 > 1$ GeV^2 59
6.3 Summary of Results on $\Delta G/G$ 61

7 Summary & Outlook **64**

A *D*-state probability in the Deuteron wave function **65**

B Relation between counting rate and asymmetry **67**

C Asymmetry Extraction **74**

D Event Weighting **77**

E Asymmetry Determination in Presence of a Polarized Background **80**

Chapter 1

Introduction

The matter we are composed of consists of protons, neutrons and electrons. Our present knowledge indicates that electrons are point-like particles without any substructure, whereas protons and neutrons, also called nucleons, have a complex substructure. The aim of this work is to investigate a special aspect of this structure, namely the polarization of gluons inside the nucleon.

A nucleon consists of quarks and gluons. Both particles can contribute to the nucleon spin of 1/2 with their intrinsic angular momentum, their spin, and their orbital angular momentum. This leads to the following sum rule

$$\frac{1}{2} = \frac{1}{2}\Delta\Sigma + \Delta G + L_q + L_g \ , \tag{1.1}$$

where $\Delta\Sigma$ is the contribution of the spin of the quarks, ΔG the contribution of the spin of the gluons, L_q and L_g the respective contributions of the quark and gluon orbital angular momentum.

Quark Models predict $\Delta\Sigma \approx 0.75$ and a simular value is obtained from an analysis of axial matrix elements of baryon decays. This is in contrast to much lower values of $\Delta\Sigma \approx 0.25$ found in polarized deep inelastic scattering. A possible explanation for this rather large difference is a large spin contribution of gluons, ΔG.

The results of the COMPASS experiment at CERN on ΔG will be presented in this work. Chapter 2 introduces deep inelastic scattering as the basic tool to study the spin structure of the nucleon. Chapter 3 reviews the so called nucleon spin puzzle, i.e. the discrepancy between small values of $\Delta\Sigma$ found in polarized deep inelastic scattering and values of $\Delta\Sigma \approx 0.75$ predicted by quark models. One possible solution to this spin puzzle would be a large value of ΔG. Ways to measure ΔG are presented in Chapter 4. Chapter 5 describes the COMPASS experiment. Chapter 6 explains the analysis, i.e. the steps from reconstructed events to the final value of the gluon polarization $\Delta G/G$. Special emphasis is put on the analysis of the open charm data set which provides the most model-independent measurement of $\Delta G/G$.

Chapter 2

Deep Inelastic Scattering

The main tool to study the (spin) structure of the nucleon is deep inelastic lepton-nucleon scattering, considering the following scattering process:

$$l + N \to l' + X \ . \tag{2.1}$$

A lepton (l) scatters off a nucleon (N). In the final state, either

- only the scattered lepton l' (inclusive process), or
- part of the hadronic final state X (semi-inclusive process),

are observed.

This process is called **deep inelastic**, if the mass of the hadronic final state M_X is larger than the masses of the nuclear resonances, i.e. $M_X \equiv W \gtrsim 2$ GeV. Most of the material presented in this chapter can be found in text books like [1, 2].

2.1 Kinematics of Deep Inelastic scattering

Fig. 2.1 shows the kinematics of the deep inelastic scattering process. The four-vectors of the particles are given in parentheses. Tab. 2.1 lists the most important kinematic variables for the inclusive process. If in addition to the scattered muon, at least one hadron is detected in the final state, additional kinematic variables are needed to define the reaction. The most important ones are listed in Tab. 2.2. Fig. 2.2 shows the relation between various kinematic variables in the $Q^2 - y$ plane for a 160 GeV muon beam.

variable	meaning
$M(m)$	nucleon (lepton) mass
$k(k')$	four vector of incoming (outgoing) lepton
$s(s')$	spin four vector of incoming (outgoing) lepton
p	four vector of nucleon in the initial state
S	spin four vector of nucleon in the initial state
p_X	four vector of hadronic final state
$E = \frac{p \cdot k}{M}$	energy of incoming lepton in laboratory system
$E' = \frac{p \cdot k'}{M}$	energy of outgoing lepton in laboratory system
θ	scattering angle of lepton in laboratory system
θ_γ	angle of virtual photon with respect to the incoming lepton in laboratory system
$q = k - k'$	four momentum transfer
$Q^2 = -q^2$	four momentum transfer squared
$\approx 4EE' \sin^2 \frac{\theta}{2}$	lepton mass neglected
$\nu = \frac{p \cdot q}{M}$	energy transfer in laboratory system
$= E - E'$	
$W^2 = (p + q)^2$	mass of hadronic final state squared
$x = \frac{Q^2}{2p \cdot q} = \frac{Q^2}{2M\nu}$	Bjorken variable ($0 \leq x \leq 1$)
$y = \frac{p \cdot q}{p \cdot k} = \frac{\nu}{E}$	relative energy transfer in laboratory system ($0 \leq y \leq 1$)
$\gamma^2 = \frac{2Mx}{Ey} = \frac{Q^2}{\nu^2}$	

Table 2.1: The most important kinematic variables and their meaning. The laboratory system is the target rest frame.

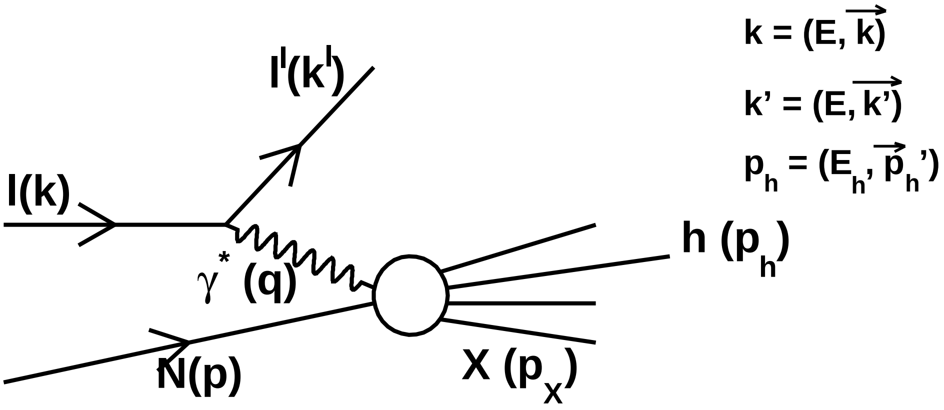

Figure 2.1: Kinematics of the deep inelastic scattering process. The four-vectors of the particles are given in parentheses.

variable	meaning
m_h	mass of observed hadron
p_h	four vector of hadron
$E_h = \frac{p \cdot p_h}{M}$	energy of hadron in laboratory system
$z = \frac{p \cdot p_h}{p \cdot q} = \frac{E_h}{\nu}$	fraction of virtual photon energy carried by the hadron in the laboratory system $(0 \leq z \leq 1)$
$p_{h\parallel} = \frac{\vec{p}_h \cdot \vec{q}}{\lvert\vec{q}\rvert}$	momentum of hadron parallel to photon momentum $\vec{q}$
$p_T = \sqrt{\vec{p}_h^{\,2} - p_{h\parallel}^2}$	transverse momentum of hadron relative to the photon
$\vec{q}^{\,*}(\vec{p}_h^{\,*})$	three vector of the virtual photon (hadron) in photon-nucleon-rest system
$p_{h\parallel}^*$	momentum of the hadron parallel to photon momentum in photon nucleon cm-system
$x_F = \frac{2}{W} \frac{\vec{q}^{\,*} \cdot \vec{p}_h^{\,*}}{\lvert\vec{q}^{\,*}\rvert} = 2\,\frac{p_{h\parallel}^*}{W}$	Feynman variable $(-1 \leq x_F \leq 1)$

Table 2.2: The most important additional kinematic variables appearing in semi-inclusive deep inelastic scattering.

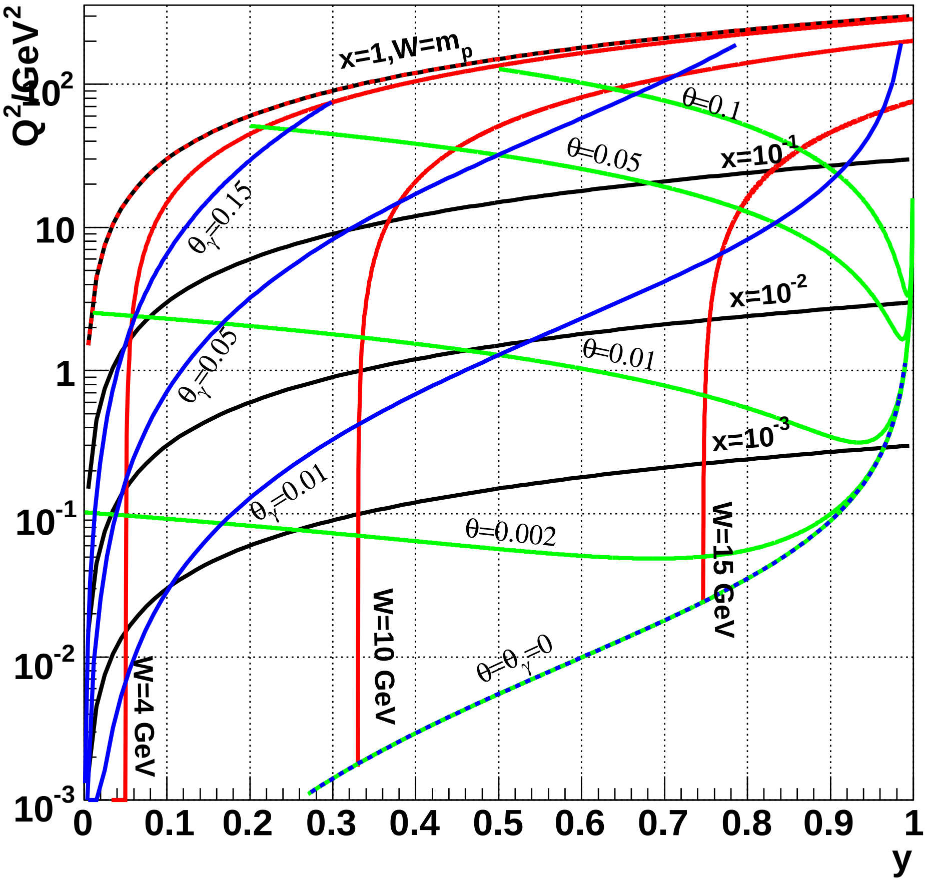

Figure 2.2: Various kinematic variables in the $Q^2 - y$ plane for a muon beam of 160 GeV momentum. The variables are explained in Tab.2.1

The inclusive cross section can be expressed in terms of kinematic variables and two structure functions carrying information about the nucleon structure:

$$\frac{d\sigma^{lN\to l'X}}{dxdy} = \frac{8\pi ME\alpha^2}{Q^4}\left[xy^2F_1(x,Q^2) + (1-y-\frac{y^2\gamma^2}{4})F_2(x,Q^2)\right]. \qquad (2.2)$$

The lepton mass was neglected in eq. (2.2). Only one photon exchange is considered here. The structure functions $F_1(x,Q^2)$ and $F_2(x,Q^2)$ depend on two variables, here chosen to be x and Q^2.

2.2 Deep Inelastic Scattering and the Quark Parton Model

In the Quark Parton Model (QPM) deep inelastic scattering is interpreted as incoherent elastic scattering off partons inside the nucleon as indicated in Fig. 2.3. The nucleon is viewed in the infinite momentum frame where each quark carries a fraction ξ of the nucleon momentum. Transverse momenta and masses are neglected. The momentum fraction ξ of the quark absorbing the virtual photon is identical to the Bjorken-variable x defined in Tab. 2.1. The structure functions have a simple probabilistic interpretation:

$$F_1(x) = \frac{1}{2}\sum_q e_q^2 q(x)\,, \qquad F_2(x) = x\sum_q e_q^2 q(x)\,. \qquad (2.3)$$

The sum extends over all active quark flavors $q = u, d, s, \bar{u}, \bar{d}, \bar{s}$ and the $q(x)$ are the unpolarized quark distributions, so that $q(x)dx$ is the number of quarks of flavor q carrying a momentum fraction in the interval $[x, x+dx]$. This interpretation is only valid for reactions where the resolution is large enough to resolve quarks inside the proton. This is the case for $Q^2 \gtrsim 1$ GeV^2 which corresponds to a resolution of $1/Q^2 \lesssim 1/\text{GeV}= 0.2$ fm. In the language of Quantum Chromo Dynamics (QCD) this means that a hard scale has to be present. For the inclusive case this is provided by $Q^2 \gtrsim 1\text{GeV}^2$. In the semi-inclusive case it may be provided either by Q^2 or the transverse momentum of a hadron with respect to the virtual photon, p_T, or the mass of a heavy quark.

The quark parton model can be extended to semi-inclusive processes. The variable z defined in Tab. 2.2 is the fraction of virtual photon energy

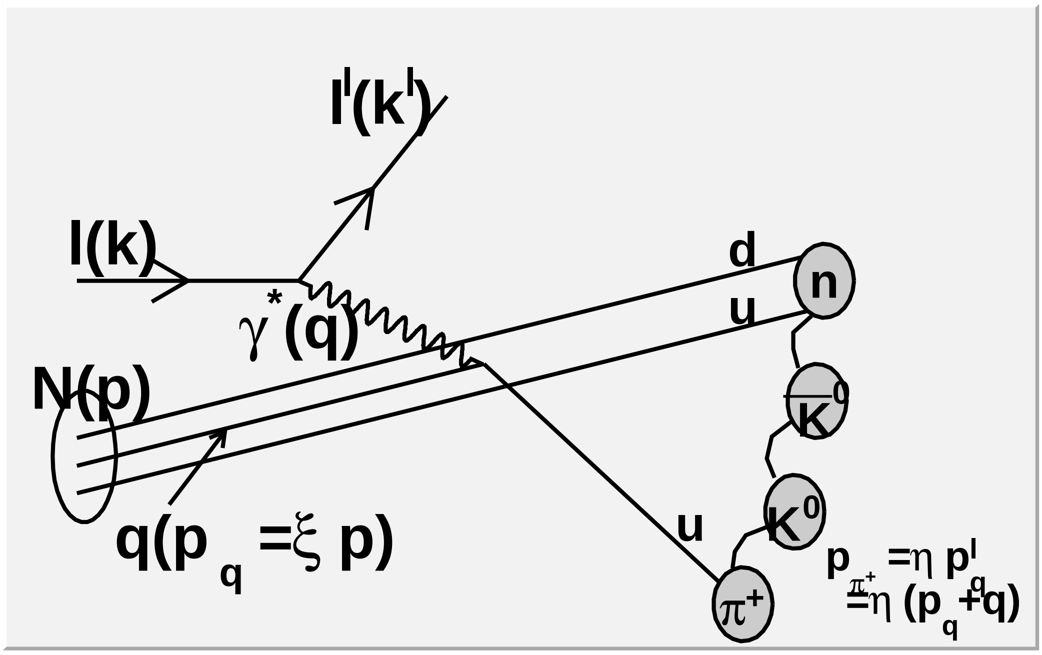

Figure 2.3: Kinematics of the deep inelastic scattering process interpreted in the Quark Parton Model (QPM). The four-vectors of the particles are given in parentheses.

carried by the hadron in the laboratory system. Intuitively it seems clear that the observation of a $\pi^+ = u\bar{d}$ at large z signals that the struck quark was most likely a u or a $\bar{d}$ quark. Formally this can be expressed by the introduction of so called fragmentation functions $D_q^h(z)$, where $D_q^h(z)dz$ is the number of hadrons of type h originating from a struck quark of flavor q in the momentum fraction range $[z, z + dz]$. In analogy to the structure function F_2 one can define:

$$F_2^h(x,z) = x \sum_q e_q^2 q(x)\ D_q^h(z) \tag{2.4}$$

and extend eq. (2.2) to the semi-inclusive case [3].

2.3 Polarization Effects in Deep Inelastic Scattering

To study the spin structure of the nucleon it is necessary to polarize the beam and the target particle. In this work only longitudinally polarized beams and targets are considered.

The cross section can be parameterized by two additional structure functions g_1 and g_2, carrying information about the spin structure of the proton. The difference of cross sections for antiparallel and parallel spins of target and beam is given by:

$$\frac{d^2\sigma^{\uparrow\downarrow}}{dxdy} - \frac{d^2\sigma^{\uparrow\uparrow}}{dxdy} = \frac{32\pi M E \alpha^2 x y}{Q^4}\left[\left(1 - \frac{y}{2} - \frac{y^2\gamma^2}{4}\right) g_1(x,Q^2) - \frac{y}{2}\gamma^2 g_2(x,Q^2)\right] . \tag{2.5}$$

Experimentally usually the cross section asymmetry

$$A^{lN} = \frac{d\sigma^{\uparrow\downarrow} - d\sigma^{\uparrow\uparrow}}{d\sigma^{\uparrow\downarrow} + d\sigma^{\uparrow\uparrow}} \tag{2.6}$$

is measured. It is given by

$$A^{lN} = D\left\{\frac{g_1 - \gamma^2 g_2}{F_1} + \eta\,\gamma\,\frac{g1 + g2}{F_1}\right\} , \tag{2.7}$$

with

$$D = \frac{y(2-y)(1+\frac{\gamma^2 y}{2})}{(1+\gamma^2)y^2 + 2(1-y-\frac{\gamma^2 y^2}{4})(1+R)}\,, \tag{2.8}$$

$$\eta = \gamma \frac{1-y-\frac{\gamma^2 y^2}{4}}{(1-\frac{y}{2})(1+\frac{\gamma^2 y}{2})} \tag{2.9}$$

$$\text{and } \gamma = \sqrt{\frac{2Mx}{Ey}} = \frac{Q^2}{\nu^2}\,, \tag{2.10}$$

where R is the ratio of longitudinal to transverse virtual photon absorption cross sections.

The lepton mass was neglected here. Since $Q^2 \ll \nu^2$, the kinematical factors η and γ are small and eq. (2.7) simplifies to

$$A^{lN} = D\,\frac{g_1}{F_1}\,. \tag{2.11}$$

The factor D is the virtual photon depolarization factor. It describes the polarization transfer from the lepton to the virtual photon. Thus g_1/F_1 can be interpreted as a photon-nucleon asymmetry

$$A^{\gamma N} = \frac{g_1}{F_1}\,. \tag{2.12}$$

In the QPM model g_1 has a simple interpretation:

$$g_1(x) = \frac{1}{2}\Sigma_q e_q^2 \Delta q(x)\,, \tag{2.13}$$

where the $\Delta q(x)$ are the polarized quark distributions:

$$\Delta q(x)\mathrm{d}x = (q^{\uparrow}(x) - q^{\downarrow}(x))\mathrm{d}x\,.$$

$\Delta q(x)\,\mathrm{d}x$ is the number of quarks with spin parallel to the nucleon spin minus the number of quarks with spin antiparallel to the nucleon spin in the momentum interval $[x, x+dx]$. The corresponding unpolarized quark distribution is given by $q(x) = q^{\uparrow}(x) + q^{\downarrow}(x)$. The QPM predicts $g_2 = 0$.

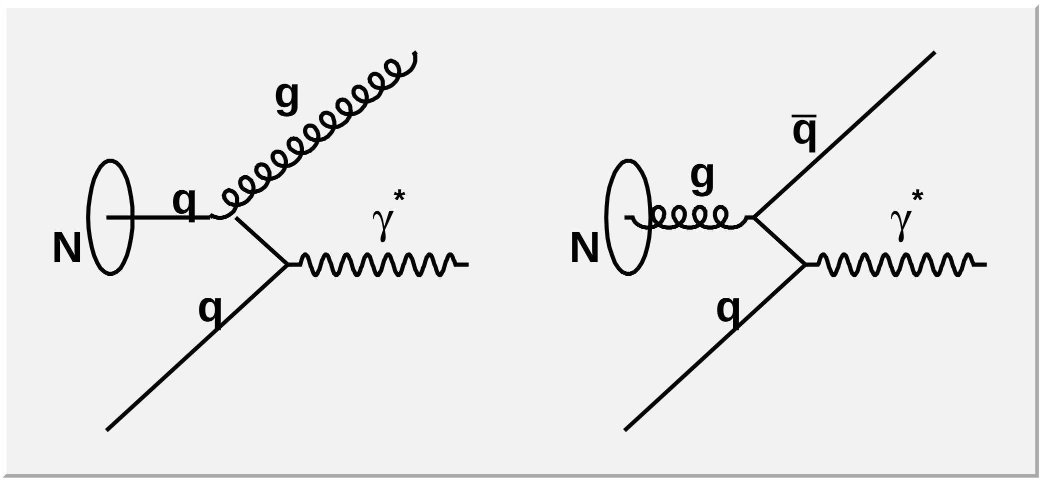

Figure 2.4: Higher order processes contributing to the cross section: The QCD Compton (left) and the photon-gluon-fusion process (right).

2.4 QCD corrections

Fig. 2.3 shows only the leading order process. At higher orders in Quantum Chromo Dynamic (QCD) other processes contribute. Two of them are shown in Fig. 2.4. One is the QCD Compton effect, where the struck quark radiates a gluon. The other one is the photon-gluon-fusion process where the photon interacts, via the creation of a quark - anti-quark pair, with a gluon. Tagging this type of process is of particular interest for measuring the gluon contribution to the nucleon spin. These processes lead to a Q^2 dependence of the structure functions and quark distributions. The leading order (LO) expressions for F_2 and g_1 read:

$$\begin{aligned} F_2(x,Q^2) &= x\,\Sigma_q e_q^2\, q(x,Q^2)\ , \\ g_1(x,Q^2) &= \frac{1}{2}\Sigma_q e_q^2\, \Delta q(x,Q^2)\ . \end{aligned} \tag{2.14}$$

For the proton structure function g_1^p one finds explicitly at LO:

$$\begin{aligned} g_1^p(x,Q^2) = \frac{1}{18}\big(&4(\Delta u(x,Q^2)+\Delta\bar{u}(x,Q^2)) + \\ &(\Delta d(x,Q^2)+\Delta\bar{d}(x,Q^2)) + \\ &(\Delta s(x,Q^2)+\Delta\bar{s}(x,Q^2))\big) \end{aligned} \tag{2.15}$$

At next to leading order (NLO) F_2 and g_1 depend in addition on the unpolarized and polarized gluon distribution $G(x) = G^{\uparrow}(x) + G^{\downarrow}(x)$ and $\Delta G(x) = G^{\uparrow}(x) - G^{\downarrow}(x)$. The NLO expression for F_2 and g_1 are given by

$$\begin{aligned} F_2(x,Q^2) &= x\sum_q e_q^2 q(x,Q^2) + \\ \frac{\alpha_s}{2\pi}\, x\sum_i e_i^2 \int_x^1 \frac{dx'}{x'} & \left(q(x',Q^2) f_q\left(\frac{x}{x'}\right) + G(x',Q^2) f_G\left(\frac{x}{x'}\right)\right) \end{aligned} \tag{2.16}$$

and

$$\begin{aligned} g_1(x,Q^2) &= \frac{1}{2}\sum_q e_q^2 \Delta q(x',Q^2) + \\ \frac{\alpha_s}{2\pi}\frac{1}{2}\sum_q e_q^2 \int_x^1 \frac{dx'}{x'} & \left(\Delta q(x',Q^2)\Delta C_q\left(\frac{x}{x'}\right) + \Delta G(x',Q^2)\Delta C_q\left(\frac{x}{x'}\right)\right) \end{aligned} \tag{2.17}$$

The coefficients f_q, f_G, ΔC_q and ΔC_g are calculable in QCD but depend, as the parton distributions do, on the renormalization procedure used.

Chapter 3

The Nucleon Spin Puzzle

This chapter reviews our knowledge about the spin structure of the nucleon starting from the simple static quark model to next to leading order (NLO) analysis of inclusive data from polarized deep inelastic scattering.

3.1 The Static Quark Model

In the static Quark Model the proton consists of two u and one d quark. Assuming an SU(2) flavor and SU(2) spin symmetry, the wave function of a proton with its spin projection pointing parallel to the quantization axis reads [4]:

$$\begin{aligned} |p\uparrow> \; &= \frac{1}{\sqrt{18}} \Big(2\,|u\uparrow u\uparrow d\downarrow> + 2\,|u\uparrow d\downarrow u\uparrow> + 2\,|d\downarrow u\uparrow u\uparrow> \\ &\quad -|u\uparrow u\downarrow d\uparrow> -|u\downarrow u\uparrow d\uparrow> -|u\downarrow d\uparrow u\uparrow> \\ &\quad -|u\uparrow d\uparrow u\downarrow> -|d\uparrow u\uparrow u\downarrow> -|d\uparrow u\downarrow u\uparrow> \Big) . \end{aligned} \tag{3.1}$$

This wavefunction allows to calculate the spin contribution of the u- and the d-quark to the nucleon spin.

$$\begin{aligned} \Delta u &= \; < p\uparrow |N_{u\uparrow}|p\uparrow> - < p\uparrow |N_{u\downarrow}|p\uparrow> = \frac{30}{18} - \frac{6}{18} = \frac{4}{3} , \\ \Delta d &= \; < p\uparrow |N_{d\uparrow}|p\uparrow> - < p\uparrow |N_{d\downarrow}|p\uparrow> = \frac{6}{18} - \frac{12}{18} = -\frac{1}{3} , \end{aligned}$$

$N_{q\uparrow}(N_{q\downarrow})$ is the operator which counts the number of quarks of flavor q with a spin projection parallel (anti-parallel) to the proton spin. Evidently in this

	p	n	Λ	Σ^+	Σ^0	Σ^-	Ξ^0	Ξ^-
μ/μ_N QM	3	-2	-0.67	2.89	0.89	-1.1	-1.55	-0.55
μ/μ_N exp.	2.79	-1.91	-0.61	2.5	–	-1.2	-1.25	-0.65

Table 3.1: Comparison of the magnetic moments in the static quark model and the experimental values. For the quark masses the following values are used: $m_u = m_d = \frac{M_p}{3}, m_s = \frac{2}{3}M_p$.

model the u and the d quark account for 100% of the nucleon spin, i.e.

$$\Delta\Sigma := \Delta u + \Delta d = \frac{4}{3} - \frac{1}{3} = 1 \ , \quad \Delta G = L_q = L_g = 0 \ . \tag{3.2}$$

Extending the SU(2) to an SU(3) flavor symmetry one can also derive the wave functions for baryons with strangeness. These allow us as well to calculate the magnetic moment of all baryons in the nucleon octet. The values obtained with the assumption $m_u = m_d = \frac{M_N}{3}, m_s = \frac{2}{3}M_p$ are shown in Tab. 3.1. They agree remarkably well with the experimental values.

3.2 Relativistic Quark Models

The static quark model predicts a value for the weak coupling constant $g_A = \Delta u - \Delta d$ of 5/3 which is about 30% above the experimental value of 1.26. In relativistic quark models quarks acquire orbital angular momentum and the value for g_A is reduced to its experimental value. Thus, in these models one typically finds:

$$\Delta\Sigma \approx 0.75 \ , \quad L_q \approx 0.125 \ , \quad \Delta G = L_g = 0 \ . \tag{3.3}$$

3.3 Baryon Decays

The first moment of the polarized quark distributions $\Delta q = \int_0^1 \Delta q(x)\ \mathrm{dx}$.[1]: is given by the following matrix element:

$$< ps|\bar{\psi}_q \gamma^\mu \gamma^5 \psi_q|ps >= (\Delta q + \Delta\bar{q})s^\mu, \tag{3.4}$$

---

[1] To simplify the notation we will often use the same symbol for a distribution $\Delta q(x)$ and its first moment $\Delta q = \int_0^1 \Delta q(x)\ \mathrm{dx}$.

where $|ps>$ describes a proton with a spin four-vector s.

This matrix element is related to the axial matrix elements of baryon decays which can be expressed, assuming SU(3) flavor symmetry, with the (generalized) Wigner-Eckhart theorem ([5],S.113)

$$< B_j|\bar{\Psi}\lambda_k\gamma^\mu\gamma^5\Psi|B_l >= if_{jkl}F + d_{jkl}D \quad j,k,l = 1\ldots 8. \tag{3.5}$$

as a function of two reduced matrix elements F and D and the $SU(3)$ structure constants f_{jkl} and d_{jkl}. B_j denotes a baryon in the baryon octet. λ_j are the generators of the $SU(3)$ group and

$$\Psi = \begin{pmatrix} \psi_u \\ \psi_d \\ \psi_s \end{pmatrix} .$$

Two of the $SU(3)$ generators are diagonal:

$$\lambda_3 = \begin{pmatrix} 1 & 0 & 0 \\ 0 & -1 & 0 \\ 0 & 0 & 0 \end{pmatrix} \quad \text{and} \quad \lambda_8 = \begin{pmatrix} 1 & 0 & 0 \\ 0 & 1 & 0 \\ 0 & 0 & -2 \end{pmatrix} . \tag{3.6}$$

The corresponding matrix elements for the proton are related to the first moment of the polarized quark distributions as follows:

$$\begin{aligned} a_3 &= (\Delta u + \Delta\bar{u}) - (\Delta d + \Delta\bar{d}) = F + D \\ &= g_A = 1.2670 \pm 0.0035 \ , && (3.7) \\ a_8 &= (\Delta u + \Delta\bar{u}) + (\Delta d + \Delta\bar{d}) - 2(\Delta s + \Delta\bar{s}) \\ &= 3F - D = 0.585 \pm 0.025 \ . && (3.8) \end{aligned}$$

Due to the group structure of $SU(3)$ the baryon decays provide only two independent measurements for the three quantities $(\Delta u+\Delta\bar{u})$, $(\Delta d+\Delta\bar{d})$ and $(\Delta s + \Delta\bar{s})$. The additional assumption $(\Delta s + \Delta\bar{s})$=0 leads to the following prediction for the helicity contributions of the quarks:

$$\Delta\Sigma = 0.585 \pm 0.025 \ , \tag{3.9}$$

which is of the same order as the prediction from relativistic quark models.

3.4 Deep Inelastic Scattering

Polarized deep inelastic scattering provides the third equation necessary to avoid the assumption $(\Delta s+\Delta\bar{s})$=0. In analogy to eq. (3.5) one can define a matrix element

$$a_0 =< B_i|\bar{\Psi}E_3\gamma^\mu\gamma^5\Psi|B_k >= (\Delta u+\Delta\bar{u}) + (\Delta d+\Delta\bar{d}) + (\Delta s+\Delta\bar{s}) = \Delta\Sigma\ . \tag{3.10}$$

accessible in DIS. E_3 is the three dimensional unity matrix. The first moment Γ_1^p of the proton structure function g_1^p can be written as:

$$\Gamma_1^p(Q^2) = \int_0^1 g_1^p(x,Q^2)\,\mathrm{dx} = \frac{1}{36}\left(4\mathrm{a}_0(\mathrm{Q}^2)+3\mathrm{a}_3+\mathrm{a}_8\right)\ . \tag{3.11}$$

In contrast to a_3 and a_8 the matrix element a_0 acquires a Q^2 dependence in the renormalization procedure due to the axial anomaly [6].

Polarized deep inelastic scattering experiments were first performed at SLAC in the 1970s [7]. The European Muon Collaboration (EMC) at CERN first determined the first moment of the spin structure function g_1^p and came to the surprising result [8, 9]:

$$\Delta\Sigma = \Delta u+\Delta\bar{u}+\Delta d+\Delta\bar{d}+\Delta s+\Delta\bar{s} \quad = \quad 0.12\pm0.17\ , \tag{3.12}$$

$$\Delta s+\Delta\bar{s} \quad = \quad -0.19\pm0.06\ . \tag{3.13}$$

This means that the helicity contribution of quarks to the nucleon spin is small and was at this time even consistent with 0! The strange quarks are negatively polarized.

This result caused the so called "spin crisis". Some physicists even casted doubt on the validity of perturbative QCD [10].

A more recent LO analysis [11] of inclusive polarized DIS data arrive at the following values

$$\Delta\Sigma \quad = \quad 0.18\pm0.04\,, \tag{3.14}$$

$$\Delta s+\Delta\bar{s} \quad = \quad -0.14\pm0.01\,. \tag{3.15}$$

This result still indicates that the helicity contribution of the quarks to the nucleon spin is small, though no longer compatible with 0, and that the strange quarks are negatively polarized.

3.5 NLO Analysis of Deep Inelastic Scattering

In NLO the matrix element a_0 is no more directly related to $\Delta\Sigma$ which depends on the renormalization and factorization scheme used. Two common choices are the $\overline{MS}$ scheme and the Adler-Bardeen (AB) scheme. In these two schemes one finds:

$$\begin{aligned} a_0(Q^2) &= \Delta\Sigma_{AB} - 3\frac{\alpha_s}{2\pi}\Delta G(Q^2)\,, && (3.16) \\ a_0(Q^2) &= \Delta\Sigma_{\overline{MS}}(Q^2)\,. && (3.17) \end{aligned}$$

The AB scheme is defined in such a way that $\Delta\Sigma_{AB}$ does not depend on Q^2, whereas $\Delta\Sigma_{\overline{MS}}$ does.

A NLO analysis [11] of inclusive polarized DIS data arrives at the following values

$$\begin{aligned} \Delta\Sigma &= 0.23 \pm 0.08\ , && (3.18) \\ \Delta s + \Delta\bar{s} &= -0.12 \pm 0.02 && (3.19) \end{aligned}$$

at $Q^2 = 1$ GeV^2. Here the so called JET scheme, similar to the AB scheme, was used.

Since the $\Delta\Sigma_{AB}$ (or $\Delta\Sigma_{Jet}$) does not depend on Q^2 it can be compared to results obtained in quark models. One solution of the spin puzzle would be that the small measured value of a_0 is explained by a cancellation of $\Delta\Sigma \approx 0.6-0.7$ as expected from quark models and analysis of baryon decays, and a large gluonic contribution ΔG. Fig. 3.1 shows $\Delta\Sigma$ and $\Delta s + \bar{\Delta} s$ as a function of ΔG. It turns out that for a very large contribution, $\Delta G \approx 2.5$, one would recover the naive expectation $\Delta\Sigma \approx 0.6$ and $\Delta s + \Delta\bar{s} \approx 0$. This is one of the motivations to determine the helicity contribution of the gluon, ΔG, to the nucleon spin.

3.5.1 Determination of ΔG from NLO QCD analysis

As shown in chapter 2, eq. (2.17) at NLO QCD the structure function g_1 depends on the polarized gluon distribution ΔG which allows in principle to determine ΔG. The NLO analysis [11] quoted above finds for the first moment:

$$\Delta G = 0.23 \pm 0.28\ . \quad (3.20)$$

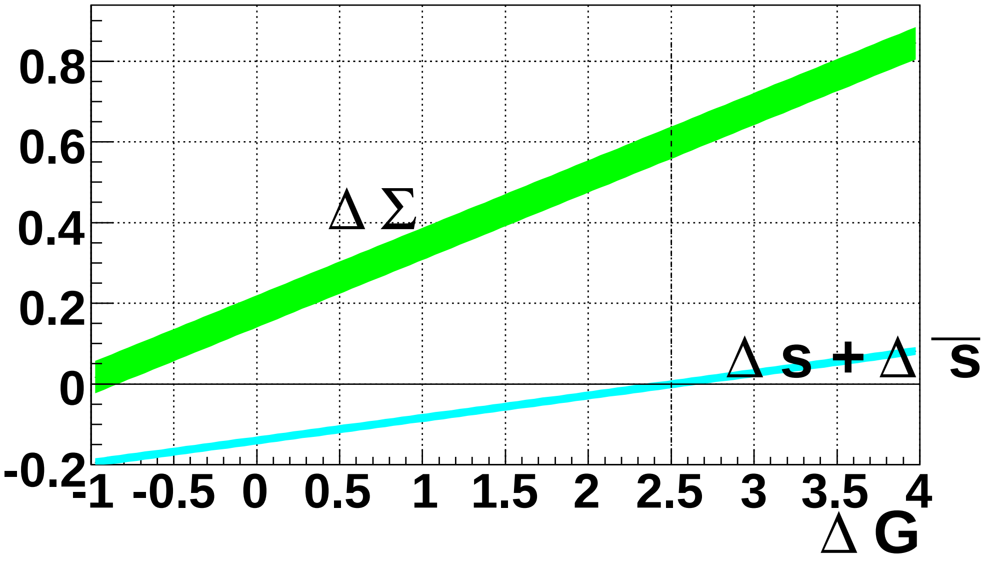

Figure 3.1: $\Delta\Sigma$ and $\Delta s + \Delta\bar{s}$ in the AB or JET scheme as a function of ΔG.

	$\Delta\Sigma$	ΔG	L_q	L_g
static QM	1	0	0	0
relativistic QM	0.75	0	0.125	0
baryon decays (assuming $\Delta s = 0$)	0.58	–	–	–
LO DIS	0.2	–	–	–
NLO DIS	0.23	$-0.5 - +0.5$	–	–

Table 3.2: Contributions of the quark and gluon spin and orbital angular momentum from different models and measurements.

at $Q^2 = 1$ GeV^2. A recent NLO analysis of the world data performed by the COMPASS collaboration [12] finds two possible solutions for the first moment ΔG at $Q^2 = 3$ GeV^2, with an equally good χ^2. One is slightly positive ($\Delta G = 0.34$), the other is slightly negative ($\Delta G = -0.31$) with an (experimental) error of the order of 0.1. Note that this error does not take into account uncertainties coming from the choice of the factorization and renormalization scale and other theoretical uncertainties. These can be much larger than the experimental error. This statement is also true for the error on ΔG in eq. (3.20). This shows that with the present available inclusive data it is difficult to determine ΔG and underlines the necessity for a direct measurement.

3.6 Summary

Tab. 3.2 summarizes the results of this chapter. After the surprising result that $\Delta\Sigma$ is small, it seems evident that the other terms in the sum rule

$$\frac{1}{2} = \frac{1}{2}\Delta\Sigma(Q^2) + \Delta G(Q^2) + L_q(Q^2) + L_g(Q^2) \tag{3.21}$$

should be measured. Especially the value of ΔG is interesting since a large value would explain the smallness of $\Delta\Sigma$.

Chapter 4

How to measure ΔG?

With deep inelastic lepton nucleon scattering as a tool, how can ΔG be measured? First of all one has to tag the partonic sub-process in which the gluon participates, shown in Fig. 4.1. This can be done by selecting some specific hadronic final states. The corresponding methods will be described in this chapter.

4.1 Open Charm Method

The intrinsic charm contribution of the proton is negligible at center of mass energies considered here, and the production of charm - anti-charm pairs out of the vacuum during the fragmentation process is highly suppressed compared to the production of lighter quark - anti-quark pairs. Charm quarks are thus almost exclusively produced via the photon-gluon-fusion process. Charm quarks fragment mainly into charmed mesons, which can be detected via their various decay channels. The observation of a charmed hadron is thus an ideal tag of the photon-gluon-fusion process. The measurement of open charm double spin asymmetries provides the most direct and model independent way to determine $\Delta G/G$.

In the analysis the following decay channel of the D^0 -meson with a branching ratio of 3.38% is used:

$$D^0 \rightarrow K^- + \pi^+ \; . \tag{4.1}$$

Since most of the D^0 are produced via the decay of their vector meson part-

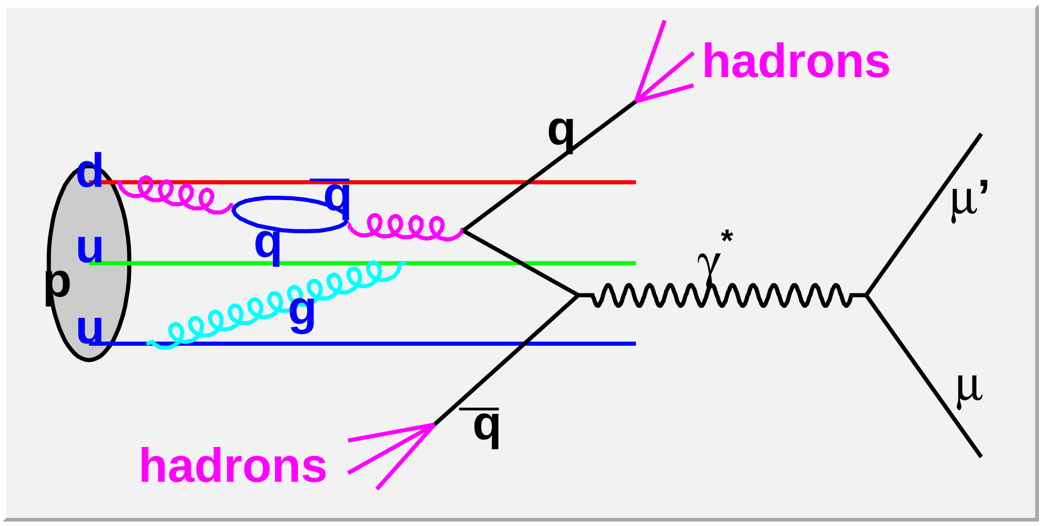

Figure 4.1: A deep inelastic event shown in the photon-nucleon CMS where the photon interacts via the photon-gluon fusion process with a gluon inside the nucleon.

ners, the decay

$$D^{*+} \rightarrow D^0 + \pi^+_{soft} \rightarrow K^- + \pi^+ + \pi^+_{soft} \tag{4.2}$$

is also considered. Experimentally this gives a better signal to background ratio. In the following, even if not explicitely mentioned, the charge conjugate decay channels are always implied.

4.2 High p_T Method

In this method one selects pairs of hadrons in the final state with large transverse momentum with respect to the virtual photon, in order to enhance the contribution of the photon-gluon-fusion process [13]. This considerably suppresses the contribution from the leading order process where hadrons are preferentially produced along the axis of the virtual photon as shown in Fig. 4.2 (left).

Compared to the open charm method the tagging of the photon-gluon-fusion process is less clean, because in the QCD Compton process (Fig. 4.2, center) hadrons are produced with a similar topology. One has to use Monte

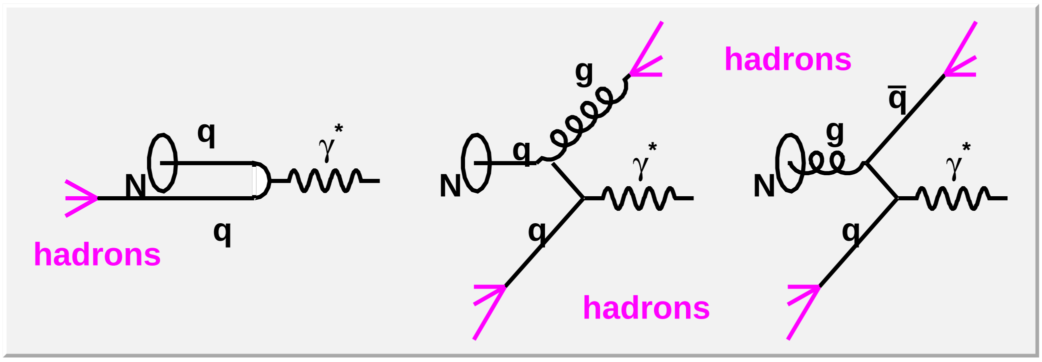

Figure 4.2: The main contributions to the cross section: Leading Order, QCD Compton and photon-gluon-fusion process.

Carlo event generators to estimate the contributions form the various subprocesses shown in Fig. 4.2. This will be discussed in more detail in chapter 6.

4.3 Comparison of the two methods

In both methods one has to measure a double spin asymmetry to extract $\Delta G/G$. The relation between the raw asymmetry, A^{raw} and $\Delta G/G$ is given by (see eq. (B.28))

$$A^{raw} = \frac{N^{\uparrow\downarrow} - N^{\uparrow\uparrow}}{N^{\uparrow\downarrow} + N^{\uparrow\uparrow}} = P_B\, P_T\, f\, a_{LL} \frac{\sigma_{PGF}}{\sigma_{PGF} + \sigma_B} \frac{\Delta G}{G} + A_B\,. \qquad (4.3)$$

Tab. 4.1 explains the variables used in eq. (4.3). With respect to eq. (B.28) the additional diluting factor $\sigma_{PGF}/(\sigma_{PGF} + \sigma_B)$ and the background asymmetry, A_B, have been added. σ_{PGF} (σ_B) is the cross section of the photon-gluon-fusion (background) process.

The polarization of the target and beam and the dilution factor are the same in both methods. The partonic asymmetry is defined as

$$a_{LL} = \frac{\sigma_{\mu g}^{\uparrow\downarrow} - \sigma_{\mu g}^{\uparrow\uparrow}}{\sigma_{\mu g}^{\uparrow\downarrow} + \sigma_{\mu g}^{\uparrow\uparrow}}$$

and depends on the following variables: $\hat{s}$, the center of mass energy of the $\gamma^* g$ system, $\cos\theta^*$, the angle of one outgoing quark with respect to the $\gamma^* - g$ axis in the center of mass system, Q^2 and y. In Fig. 4.3 a_{LL} is shown as a function of $\hat{s}$ for $y = 0.5$, $Q^2 = Q^2_{min} = m^2y^2/(1-y) \approx 5.5 \cdot 10^{-3}\mathrm{GeV}^2$ integrated over $\cos\theta^*$. The values obtained for light quark production and for $c\bar{c}$ production are very different.

For heavy quarks, the asymmetry is positive at threshold ($= 4m_c^2$) and turns to negative values at large $\hat{s}$. For light quarks, the asymmetry is negative for all values of $\hat{s}$. Leading order expressions for the partonic asymmetry a_{LL} used in the analysis can be found in [14]. Note that the term "Leading order" is confusing here, since at leading order in the sense of $\alpha_s = 0$ there is no PGF process. Leading order thus means here the first non-vanishing order.

We now turn to the fraction of signal events, $\sigma_{PGF}/(\sigma_{PGF} + \sigma_B)$. In the high p_T analysis it has to be determined from a MC simulation and is of the order of 0.3 (see chapter 6). In the open charm analysis it depends on the experimental resolution of the D^0 reconstruction. It is of the order of 0.1 for the direct D^0 decay and of the order of 0.5 for the decay via a D^* as will be shown in chapter 6. More important than these numerical differences is the fact that in the open charm method the signal fraction can be determined directly from the data in a model independent way, whereas in the high p_T method one has to trust the underlying model of the MC generator.

4.3.1 Gluon momentum fraction x_g

In the leading process order the Bjorken variable x is identical to the momentum fraction carried by the struck quark in the nucleon. This can be seen from the left picture in Fig. 4.2 by looking at the energy-momentum conservation at the vertex:

$$\begin{aligned} x_q P + q &= p_{q'} \\ \Rightarrow &\quad m_q^2 + 2x_q P \cdot q - Q^2 = m_q^2 \\ \Rightarrow &\quad x_q = \frac{Q^2}{2P \cdot q} \equiv x \; . \end{aligned} \tag{4.4}$$

The last equation shows that the momentum fraction of the quark (x_q) is identical to the Bjorken variable x.

In a NLO process, like photon-gluon-fusion, one does not have direct

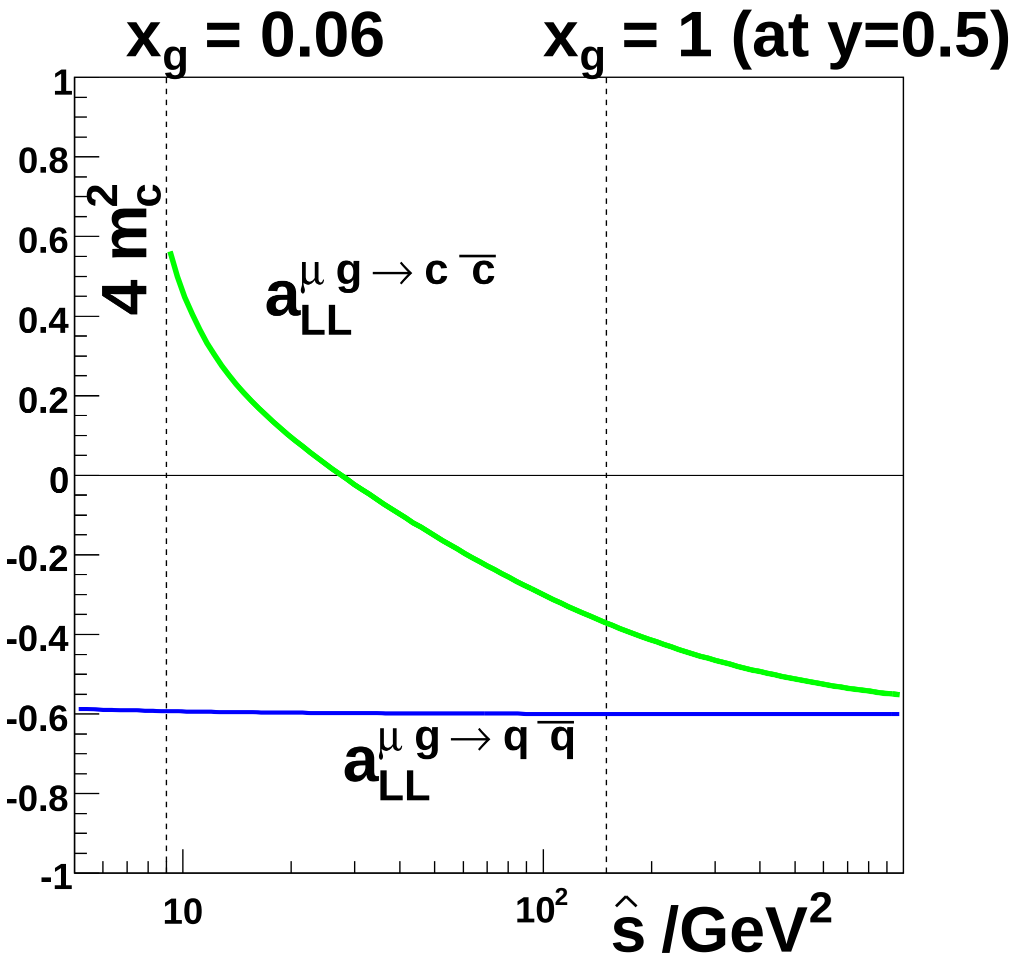

Figure 4.3: The partonic asymmetry a_{LL} as a function of the CMS energy of the photon-gluon system. The values of the other variables are $Q^2 = 0.01$ GeV^2, $y = 0.5$. An integral over $\cos\theta^*$ is performed.

	high p_T	open-charm
$N^{\uparrow\downarrow}(N^{\uparrow\uparrow})$	number of	
	high p_T	open charm
	events with beam and target	
	spin parallel (antiparallel)	
$P_B \approx -0.8$	beam polarization	
$P_T \approx 0.5$	target polarization	
$f \approx 0.4$	dilution factor (^{6}LiD target)	
a_{LL}	asymmetry of partonic process	
	≈ -0.6	-0.6 to 0.6
$\frac{\sigma_{PGF}}{\sigma_{PGF}+\sigma_B}$	fraction of photon-gluon fusion process	
	0.3	$0.5(D^*)$ 0.1 (D^0)
	estimated from	
	LEPTO/PYTHIA MC	invariant mass spectrum
A^B	background asymmetry	

Table 4.1: Definition of the variables used in eq. (4.3) and their meaning.

access to the momentum fraction carried by the gluon, x_g:

$$\begin{aligned} x_g P + q &= p_q + p_{\bar{q}} = \hat{s} \\ &\Rightarrow \quad 2x_g P \cdot q - Q^2 = \hat{s} \\ &\Rightarrow \quad x_g = \frac{\hat{s}+Q^2}{2P\cdot q} = \frac{\hat{s}+Q^2}{2M\nu}\ . \end{aligned} \tag{4.5}$$

The CMS energy of the partonic subprocess, $\hat{s}$, cannot be calculated from the kinematics of reconstructed particles. This means that the measurements of $\Delta G/G$ presented here always measure $\Delta G/G$ in a certain range of x_g which has to be determined from a MC simulation. The kinematics of the reconstructed hadrons can be used to get an approximate value of x_g as was shown in [13].

4.4 Other ways to measure ΔG

Another possibility to determine the gluon polarization is to use polarized proton-proton scattering. Here the partonic subprocesses are

- quark-quark,
- quark-gluon and
- gluon-gluon

scattering. As in deep inelastic scattering, various final states are considered to tag subprocesses where the gluon participated. Double spin asymmetries are sensitive to ΔG (or even ΔG^2 in case of the gluon-gluon subprocess). Such experiments are performed at the Relativistic Heavy Ion Collider (RHIC) at Brookhaven National Laboratory (BNL) in New York.

One advantage with respect to deep inelastic scattering is the higher available center of mass energy (up to $\sqrt{s} = 200$ GeV at the moment) compared to $\sqrt{s} = \sqrt{2ME} = \sqrt{2 \cdot 0.938 \cdot 160} = 17$ GeV for the COMPASS muon beam. This makes the perturbative QCD analysis of the data more reliable. On the other hand, the presence of two hadrons in the initial state makes the interpretation of the data more difficult compared to deep inelastic scattering where the nucleon is probed with a point-like particle.

Chapter 5

The COMPASS Experiment

The previous chapters showed that in order to study the spin structure of the nucleon, in particular the gluon spin contribution, the requirements are

- a high energy polarized lepton beam
- a polarized nucleon target
- a detector with good particle identification to detect the scattered lepton and the produced final state hadrons

COMPASS uses a polarized 160 GeV muon beam. Advantages as compared to an electron beam for example are the higher available energies and the natural polarization. As target material serves ^{6}LiD. To cover a large momentum range of the final state particles, COMPASS uses a two stage spectrometer with good particle identification. In this chapter the various components of the COMPASS experiment will be presented.

5.1 History

The COMPASS (**CO**mmon **M**uon and **P**roton **A**pparatus for **S**tructure and **S**pectroscopy) collaboration was formed in 1996 from the merge of two proposed experiments at the CERN M2 beam-line. The first one, CHEOPS, proposed to study physics with hadron beams, like the measurement of pion and kaon polarizabilities and the search for glueballs, hybrids and double charmed baryons. The other one, called HMC (**H**adron **M**uon **C**ollaboration) at the time (in line with the predecessor experiments EMC, NMC, SMC) proposed to study the nucleon spin structure. In 1997 CERN approved the COMPASS proposal [15] as CERN experiment NA58. The collaboration comprises about 200 physicists. Construction took place in the years 1998-2000. A commissioning run was performed in 2001. This work describes the results from physics runs with a muon beam in 2002, 2003 and 2004. The experiment was upgraded in 2005 and data taking was continued in 2006.

5.2 Beam

The Super-Proton-Synchrotron (SPS) accelerates protons to a momentum of 400 GeV. Every 15s approximately 10^{13} protons are extracted during 5 s and hit a beryllium target. A magnet system selects pions and kaons produced at this target within a given momentum range. In a 600 m long decay line a fraction of these hadrons decays into muons which are naturally polarized due to the parity violating character of the decay. Remaining hadrons are absorbed at the end of the decay channel. The produced muons are selected according to their momentum. Muon momenta up to 280 GeV can be chosen. COMPASS runs with a 160 GeV μ^+ beam with a momentum spread of $\sigma_p/p \approx 5\%$. The intensity is 2×10^8 muons/spill of 5s. The momentum of single beam muons is measured to a precision of $\Delta p/p = 0.8\%$ with help of scintillator hodoscopes placed before and behind the last vertical bending magnet. The polarization of the muon beam was determined by a Monte Carlo simulation. In 2004 it was found to be in average $P_B = -0.80 \pm 0.04$. In the analysis the beam polarization is calculated event by event according to the beam momentum.

Only 70% of these muons hit the 3 cm diameter target cells. The remaining 30% consist of particles far away from the beam axis, with momenta lower than the nominal beam momentum and large angles with respect to the beam axis. This so called halo is typical for a tertiary beam like a muon beam.

5.3 Polarized Target

Until the end of 2004 COMPASS has used a polarized solid state target already in operation in the predecessor experiment SMC. Its main components are (Fig. 5.1):

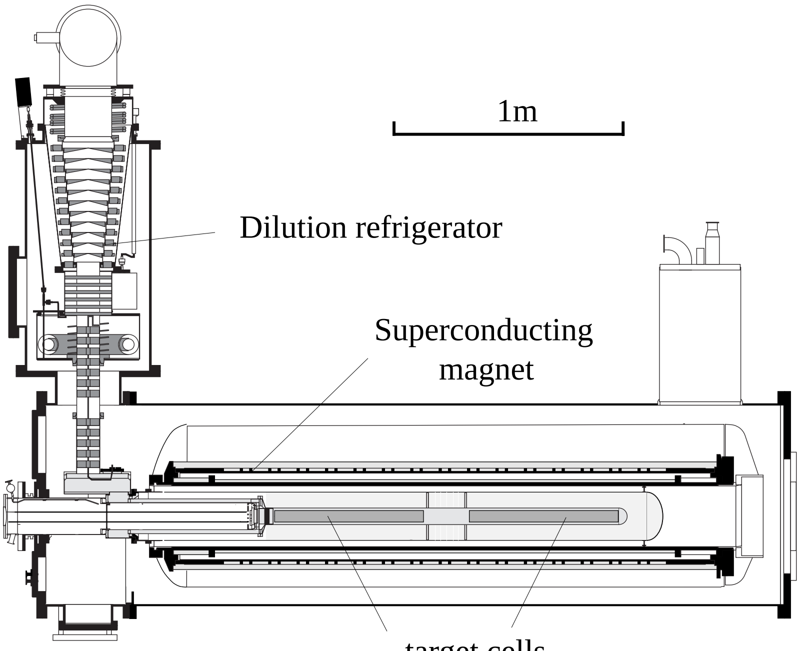

Figure 5.1: The polarized target.

- two cylindrical target cells filled with ^{6}LiD,
- a ^{3}He-^{4}He dilution refrigerator,
- a solenoid and dipole magnet,
- a microwave system to polarize the nucleons, by dynamic nuclear polarization (DNP),
- an NMR system to measure the polarization.

The two cells have a diameter of 3 cm and are 65 cm long. The cells are separated by 10 cm. They are oppositely polarized in order to limit the systematic error in the asymmetry extraction. As target material ^{6}LiD is used since it maximizes the figure of merit, i.e. the square of the product of dilution factor f and target polarization P_T. The dilution factor f is defined as the fraction of polarizable nucleons in the target material. The ^{6}Li nucleus can be considered as spin 0 ^{4}He nucleus plus a deuteron. With the additional D in ^{6}LiD the dilution factor is 50%. Additional material like liquid helium and NMR coils lead to a further dilution, so that the final dilution factor is about 40%. The target material is polarized via dynamic nuclear polarization (DNP) to approximately 55%. The polarization is measured with NMR coils inside the target cells. The relative error of the measurement is 5%. Because of the D-state contribution of $\omega_D = 5\%$ [16] in the deuteron wave function, the polarization of the nucleons inside the deuteron is reduced by a factor of $1/(1-1.5\omega_D)$ with respect to the deuteron polarization (see App. A). In the following this correction is included in the values for the target polarization P_T used in the analysis.

A ^{3}He-^{4}He dilution refrigerator allows to cool down the system to 50 mK. A superconducting solenoid provides a 2.5T magnetic field along the beam direction with a axial homogeneity better than 20ppm. In this longitudinal mode the target material can constantly be repolarized during data taking. A transverse 0.5T field is produced by a dipole magnet. It allows running in a transverse mode and changing the orientation of the target spins with respect to the beam in approximately 20 min without repolarizing the target material. These field reversals are performed approximately every 8 h.

5.4 Spectrometer

COMPASS uses a two stage spectrometer shown in Fig. 5.2. The large angle spectrometer (LAS) covers an aperture of ±180 mrad, whereas the small angle spectrometer (SAS) covers ±30 mrad. Both stages consist of a spectrometer magnet with field integrals of 1 and 4.4 Tm for the LAS and SAS, respectively. The spectrometer magnets are preceeded and followed by various tracking detectors listed in Tab. 5.1. The LAS is equipped with a Ring Imaging Cherenkov Counter (RICH) as well as a hadronic calorimeter. The SAS includes an electromagnetic and hadronic calorimeter. Both stages are equipped with hadron absorbers allowing muon identification in tracking detectors located downstream. The trigger system, based on the detection of the scattered muon, will be described in detail in the next section.

Tracks from approximately 1 GeV up to the incident beam momentum can be reconstructed. The relative momentum resolution σ_p/p is 0.5% for high momentum tracks ($p > 10$ GeV) reconstructed in both spectrometers and approximately 1.2% for low momentum tracks. The RICH allows a pion/kaon separation at the 2.5 σ level up to 40 GeV. The threshold for kaon detection is at 9 GeV.

Detector	purpose: tracking of ...
Scintillator Hodoscopes (**B**eam **M**omentum **S**tation)	incoming muon
Silicon	incoming muon
Scintillator hodoscopes	particles downstream of the target in the beam region
Gaseous **E**lectron **M**ultiplier (GEM) **MICRO ME**sh **GA**seous **S**tructure (Micro Megas)	small angle tracks
MWPC Drift Chamber Straws (large area drift tubes)	large angle tracks
Muon Walls (drift tubes)	muon behind hadron absorbers

Table 5.1: Tracking detectors used in the COMPASS experiment.

A detailed description of the spectrometer can be found in [17].

5.5 Trigger System

As described in section 5.2 the muon beam has an intensity of 2×10^8/spill with a considerable halo component. The rate of useful scattering events is about 10^4/spill. The task of the trigger system is to identify these events within a decision time below 500 ns, in order to start the detector readout system and to provide a time reference for other detectors.

Two types of reactions are of interest:

$$\begin{array}{lcll} \mu + N & \rightarrow & \mu' + X & \text{inclusive reaction} \\ \mu + N & \rightarrow & \mu' + h + X & \text{semi-inclusive reaction} \end{array}$$

Common to both is the appearance of a muon in the final state. It seems thus natural to base the trigger decision on the detection of the scattered muon, especially because the muon can easily be identified online by hits in detectors located behind the hadron absorber. COMPASS uses scintillator hodoscope pairs where at least one hodoscope of the pair is placed behind a hadron absorber to identify the scattered muon. The location of these

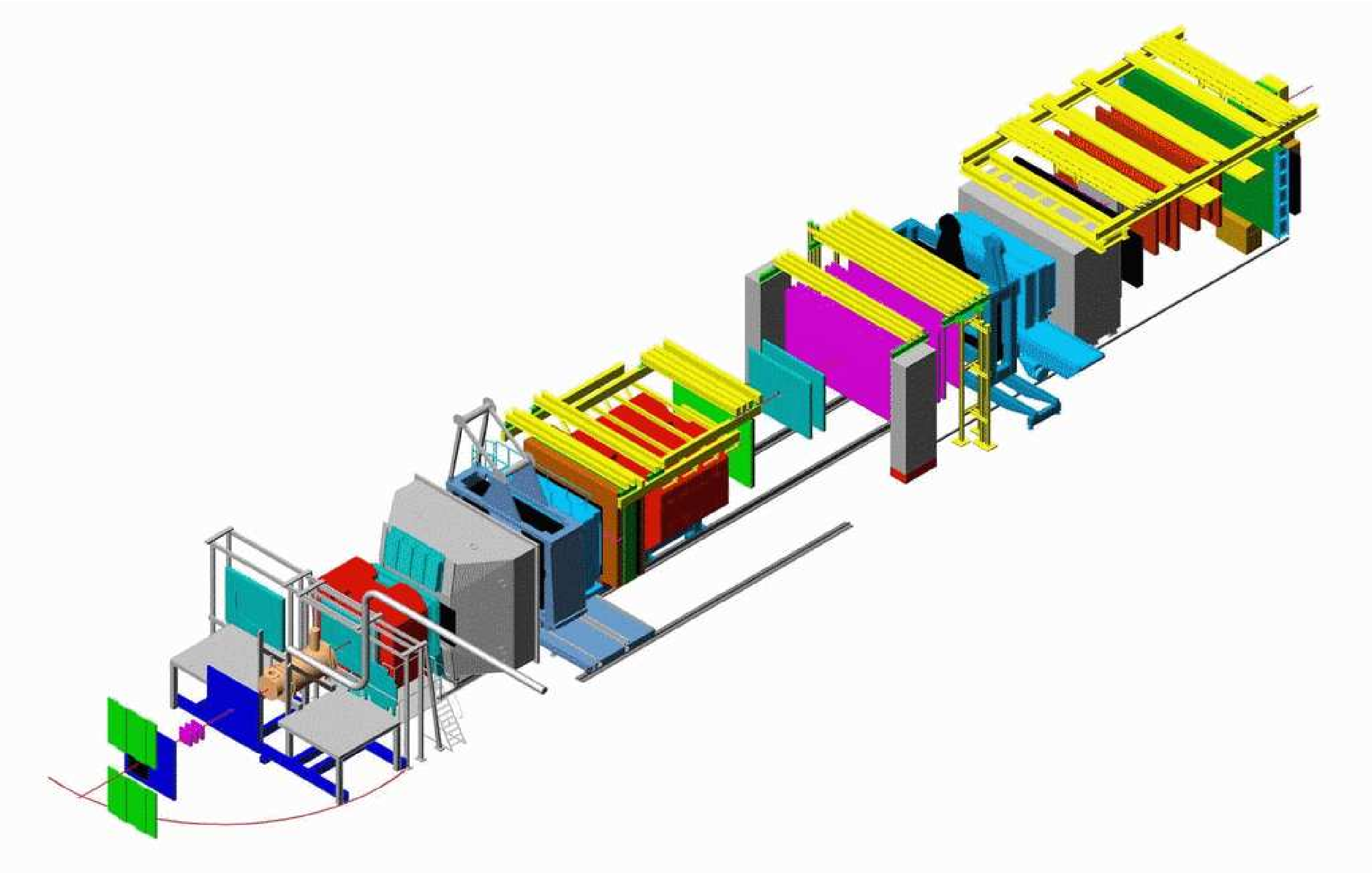

Figure 5.2: The COMPASS spectrometer.

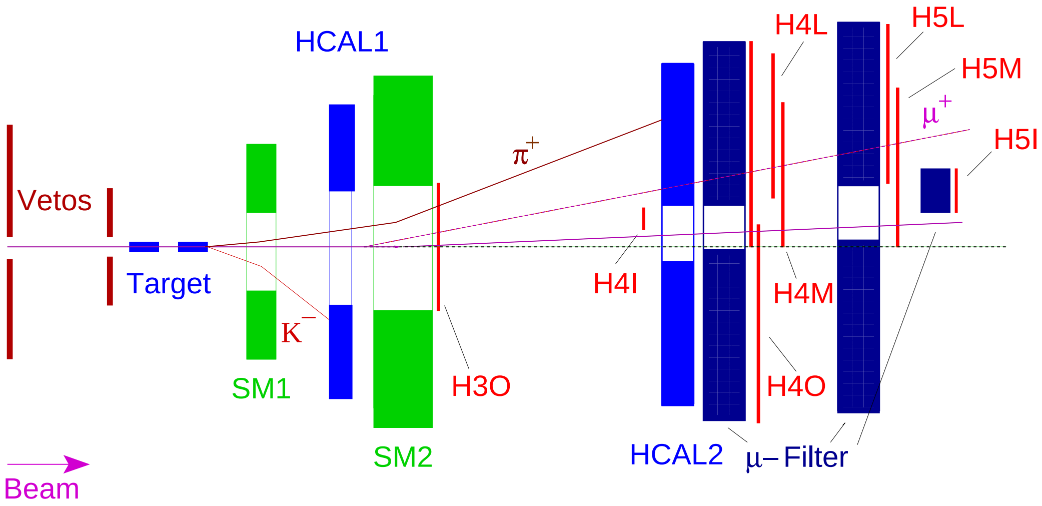

Figure 5.3: Position of the hodoscopes in the spectrometer. There are in total four subsystems: H4I & H5I, H4M & H5M, H4L & H5L and H3O & H4O.

hodoscopes is shown in Fig. 5.3. The granularity of the hodoscopes allows to select muons pointing back to the target region in the non-bending plane or to select muons with a minimal energy loss in the bending plane. Not all combinations of hits in the first and the second plane lead to a trigger signal. Fig. 5.4 shows a simplified picture in the non bending plane. The muon labeled μ_1 interacts in the target and hits both hodoscopes. The same is true for the halo muon μ_2, which can however be eliminated by accepting only those combinations of strips in the two hodoscopes which point back to the target. This is realized by so called coincidence matrices shown on the right in Fig. 5.4. The gray matrix elements stand for the allowed coincidences. Note that in reality the hodoscopes have 16-32 strips and the matrices have 32 rows and columns and allow thus to select up to 1024 coincidences.

Unfortunately it is impossible to base the trigger decision on the scattered muon alone. The trigger rates are about two orders of magnitude higher than expected from the cross section of the interesting events if one just asks for an allowed coincidence in a pair of hodoscopes. This is because a considerable fraction of the halo muons like μ_3 and μ_4 in Fig. 5.4 cause a trigger signal as well, without interacting in the target. Fig. 5.4 also shows how these unwanted signals can be eliminated: by placing additional veto hodoscopes in front of the target and demanding that no signal was present.

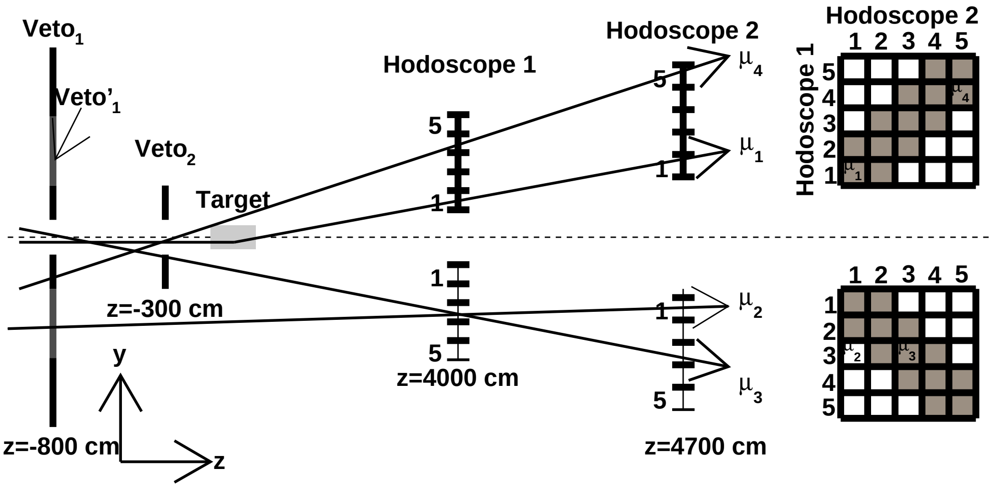

Figure 5.4: μ_1 interacts in the target and fulfills the trigger condition by hitting both hodoscopes and the matrix condition. The halo muons μ_2, μ_3 and μ_4 are vetoed by causing a signal in one of the veto hodoscopes placed upstream of the target.

This eliminates trigger signals from the muons μ_3 and μ_4. Fig. 5.4 illustrates as well the need for two veto hodoscopes placed at two different z-positions along the beam-line. One hodoscope is not sufficient to eliminate both μ_3 and μ_4. One disadvantage of such a veto system is the dead time associated with it. A halo muon hitting one of the veto counters, even if it does not cause an allowed coincidence in the trigger hodoscopes (like μ_2), will prohibit a trigger signal for typically 15 ns. The total rate seen by the veto system is approximately 15 MHz. This results in a dead time of the order of 15ns $\times$ 15 MHz $\approx$ 20%.

A second possibility to reduce the contribution from trigger signals caused by halo events is to demand, in addition to the hodoscope signal, a signal above a certain threshold (typically 3 times the most probable energy loss of a minimal ionizing particle) in the hadron calorimeters. This has also the advantage to suppress unwanted events like elastic muon electron scattering:

$$\mu + e^- \rightarrow \mu' + e^- \ ,$$

or radiative events

$$\mu + N \rightarrow \mu' + N + \gamma \ .$$

The disadvantage of this method is, that it may introduce some bias in the selection of inclusive events. The hadron calorimeters do for example have different detection probabilities for positive, negative or neutral hadrons. It is thus desirable to avoid using this information for the measurement of inclusive asymmetries.

The trigger system is set up in such a way that the 3 subcomponents

- Hodoscope system,
- veto system,
- Calorimeter trigger

can be combined individually for every hodoscope subsystem. Hodoscope systems in a kinematic region with large contributions from background events are complemented by the calorimeter trigger. Hodoscopes which cover the acceptance at large Q^2, where the inclusive asymmetries are of special interest, use only the veto system. The veto system itself is subdivided in two subsystems: In V_{tot} all veto counters are included (also a veto hodoscope further upstream in the beam-line not shown in Fig. 5.4) in V' only part of the veto counters are included, resulting in a reduced dead time of about 6%. To trigger also on events at very large Q^2 where no hodoscope is available, a so called pure calorimetric trigger is used. Here the threshold is set to approximately 10 GeV. The kinematic regions covered by the various trigger subsystems are shown in Fig. 5.5.

Table 5.2 shows the trigger rates obtained with different settings of the hodoscope systems and the pure calorimeter trigger. The settings used during the data taking are shown in **bold face**. This choice was driven by the limit of the data acquisition system of about 50000 triggers/spill. The purity of the trigger, i.e. the ratio of "good triggered" events and triggered events is approximately (15%) 35% for triggers (not) including calorimetric information.

More technical details about the trigger system can be found in [18].

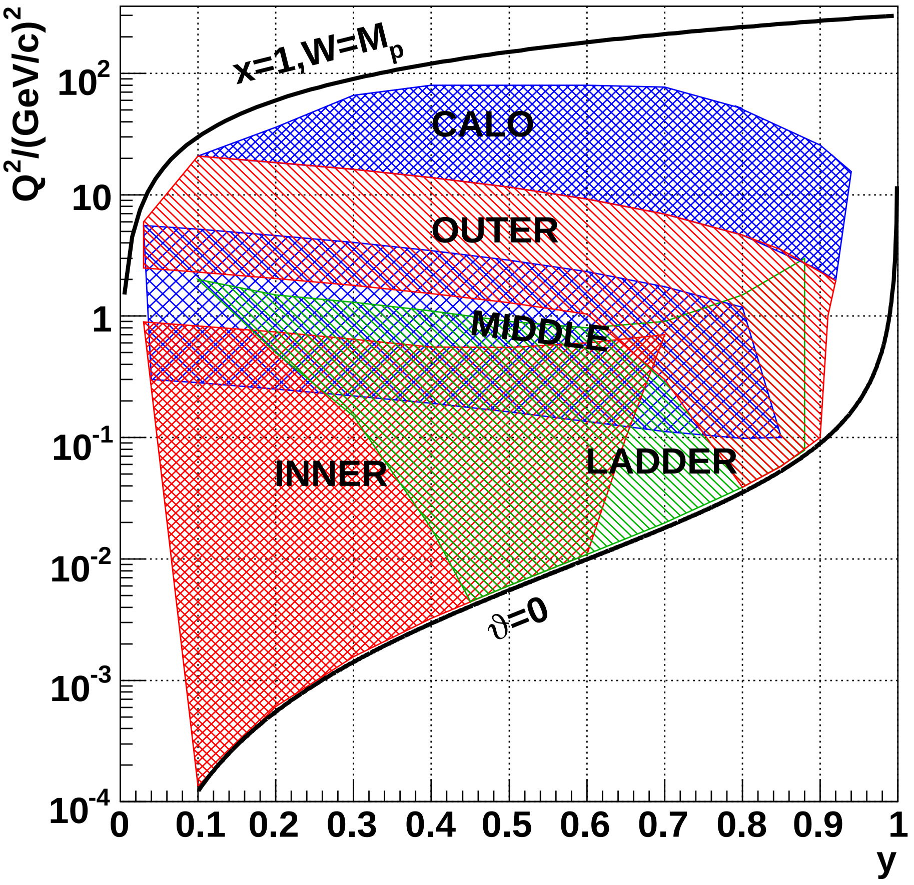

Figure 5.5: The kinematic regions covered by the different trigger subsystems.

Trigger		$\overline{V'}$	$\overline{V_{\text{tot}}}$	Calo	Calo $\times\overline{V'}$	Calo $\times$ $\overline{V_{\text{tot}}}$
Inner	1049	513	219	**11**	8	5
Ladder	564	114	34	26	**6**	3
Middle	1400	120	**20**	50	4	**1**
Outer	899	28	**8**	54	2	0.6
pure Calo.	106	27	**5**	-	-	-

Table 5.2: Trigger rates in 1000/spill for different trigger settings. The actually chosen trigger settings are shown in **bold face**. The beam intensity was 2×10^8 muons per spill. The middle trigger was once recorded in coincidence with the calorimeter and once without. The latter was prescaled by a factor 2.

Chapter 6

Analysis & Results

COMPASS collects a few hundred Terabyte of raw data every year. After calibration and alignment procedures so called mini data summary tapes (mDST) are produced. They amount to approximately 1 TB/year and contain all the relevant information to perform a physics analysis. This chapter describes the steps from the reconstructed events to the extraction of $\Delta G/G$. Data from the years 2002, 2003 and 2004 are included in this analysis.

6.1 Open Charm Analysis

6.1.1 Event Selection

Only events with a reconstructed primary vertex are considered. This implies the reconstruction of the beam muon and the scattered muon. In addition the vertex position has to be inside one of the two target cells.

As mentioned in section 4.1, one has to identify events with charmed hadrons in the final state. COMPASS looks at the following decay channels (including their charge conjugates):

$$D^0 \rightarrow K^- + \pi^+ \tag{6.1}$$

and, since most of the D^0 are produced via the decay of the vector meson partners,

$$D^{*+} \rightarrow D^0 + \pi^+_{soft} \rightarrow K^- + \pi^+ + \pi^+_{soft} \; . \tag{6.2}$$

After applying cuts specified in Tab. 6.1 to optimize the statistical significance of the measurement one obtains the mass spectra shown in Figs. 6.1

	D^0	D^*
z_{D^0}	> 0.2	> 0.25
$\cos\theta^*$	< 0.85	< 0.5
δm	–	3.1 MeV $< (\delta m - m_\pi) <$ 9.1 MeV
	Kaon identified in RICH	

Table 6.1: Cuts used to select the D^0 and D^* sample: δm is the difference between the reconstructed D^* and D^0 masses, i.e. $\delta m = M_{D^*} - M_{D^0}$ and θ^* the angle of one of the decay particles in the D^0 rest-frame with respect to the direction of the D^0 in the laboratory system.

and 6.2. A discussion on optimizing these cuts can be found in [19, 20]. Events appearing in Fig. 6.2 don't enter the spectrum in Fig. 6.1.

The D^0 mass spectrum is fitted to

$$f(m) \quad = \quad \frac{A_1}{\sqrt{2\pi}\sigma_1}\,\mathrm{e}^{\frac{-(m-m_1)^2}{2\sigma_1^2}} + A_2\,\mathrm{e}^{\frac{-m}{s_2}} + (1 + p_1 m + p_2\, m^2)\ , \qquad (6.3)$$

and the D^* mass spectrum to

$$f(m) \quad = \quad \frac{A_1}{\sqrt{2\pi}\sigma_1}\,\mathrm{e}^{\frac{-(m-m_1)^2}{2\sigma_1^2}} + \frac{A_2}{\sqrt{2\pi}\sigma_2}\,\mathrm{e}^{\frac{-(m-m_2)^2}{2\sigma_2^2}} + A_3\,\mathrm{e}^{\frac{-m}{s}} \qquad (6.4)$$

where the second Gaussian accounts for the bump centered at $m \approx -250$MeV originating from decays

$$D^0 \to K^- + \pi^+ + \pi^0$$

where the π^0 was not reconstructed.

6.1.2 Determination of $\Delta G/G$

The following section describes in detail how the value for $\Delta G/G$ is extracted from the reconstructed charmed mesons. This seems to be straightforward using eq. (4.3):

$$\begin{aligned} A^{raw} &= \frac{N^{\uparrow\downarrow} - N^{\uparrow\uparrow}}{N^{\uparrow\downarrow} + N^{\uparrow\uparrow}} \\ &= P_B\, P_T\, f\, a_{LL} \frac{\sigma_{PGF}}{\sigma_{PGF} + \sigma_B} \frac{\Delta G}{G} + A^B\ , \end{aligned}$$

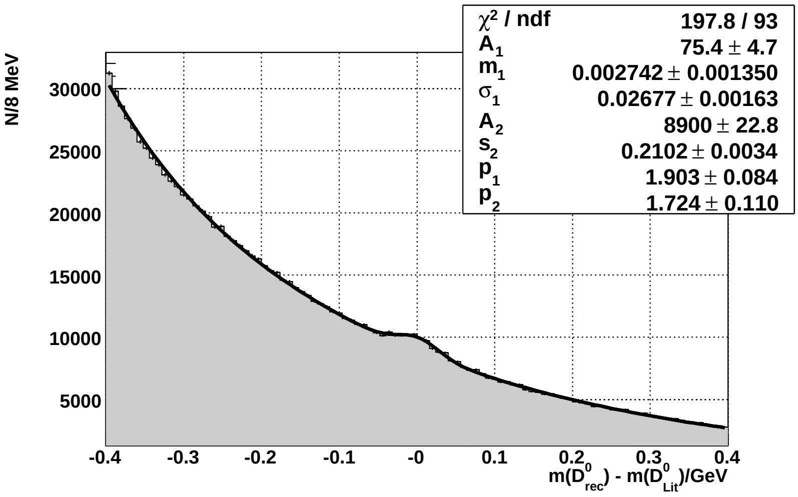

Figure 6.1: Invariant mass spectrum of $K^-\pi^+$ and $K^+\pi^-$ pairs of 2004 data with cuts as given in the second column (D^0) of Tab. 6.1.

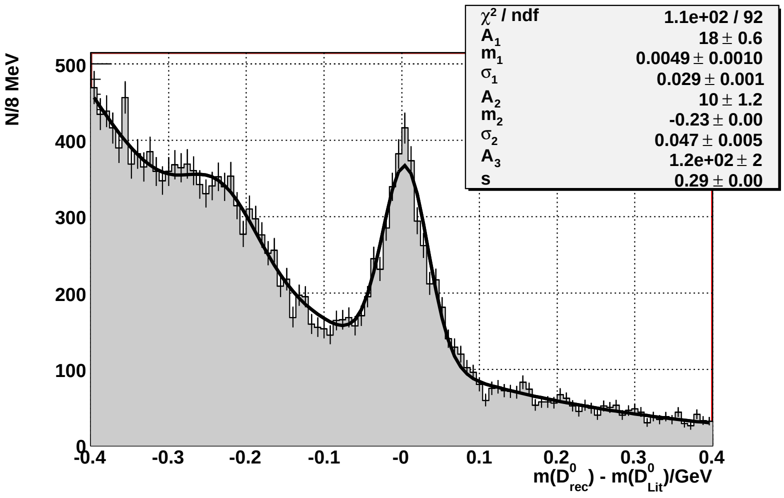

Figure 6.2: Invariant mass spectrum of $K^-\pi^+$ and $K^+\pi^-$ pairs of 2004 data with cuts given in the third column (D^*) in Tab. 6.1.

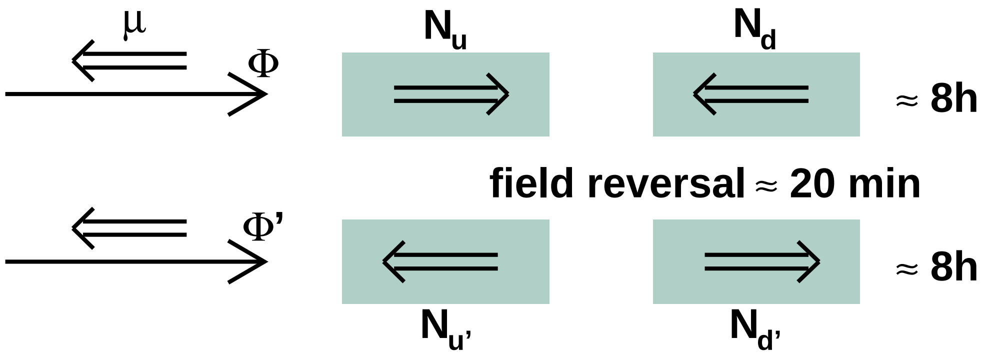

Figure 6.3: To extract the asymmetry four measurements of event rates ($N_u, N_d, N_{u'}$ and $N_{d'}$) are used. The double arrows indicate the direction of the polarization vector.

knowing all the factors in front of $\Delta G/G$ and the background asymmetry, A_B, but acceptance effects and flux normalization were ignored in eq. (4.3).

Extracting $\Delta G/G$ without knowledge of flux and acceptance

To extract $\Delta G/G$ using only minimal assumptions on the beam flux Φ and the acceptances a, four sets of data are used as shown in Fig. 6.3. First data are taken for approximately 8 hours with the first setting of target polarization resulting in two rates N_u and N_d of events with the vertex reconstructed in the up and downstream target cell, respectively. Then the magnetic field of the target is reversed, resulting in a change of sign of the target polarizations with respect to the beam. In this setting data are again taken for about 8 hours. The corresponding event rates are $N_{u'}$ and $N_{d'}$. For each of these so called configurations of about 16 hours the asymmetry can be extracted. The high p_T analysis follows this procedure. In the open charm analysis, due to the limited statistics, data are grouped together in larger configurations of about one week. A detailed description of the data selection and grouping used in this analysis can be found in [20].

The relation between the event rates N_t and $A_S \equiv \Delta G/G$ is given by eq. (C.1) in App. C:

$$N_t \quad = \quad \alpha_t \,(1- <\beta_t> A_S) \qquad t = u, d, u', d' \tag{6.5}$$

with

$$\begin{aligned} \alpha_t &= \int a_t \Phi_t n_t \sigma_t \mathrm{d}^n x \quad \text{and} & (6.6) \\ \beta_t &= P_B P_{T,t} f_t a_{LL} \frac{\sigma_{PGF}}{\sigma_{PGF} + \sigma_B} \; . \end{aligned}$$

In eq. (6.6) n_t denotes the number of target nucleons and $\sigma_t = \sigma_{PGF} + \sigma_B$ the unpolarized cross section. The integral $\mathrm{d}^n x$ extends over all accepted events.

If we ignore for the moment a possible contribution from the background asymmetry A_B, the asymmetry A_S can be extracted from

$$\delta = \frac{N_u N_{d'}}{N_{u'} N_d} = \frac{\alpha_u \alpha_{d'}}{\alpha_{u'} \alpha_d} \frac{(1- <\beta_u> A_S)(1- <\beta_{d'}> A_S)}{(1- <\beta_{u'}> A_S)(1- <\beta_d> A_S)} \; , \tag{6.7}$$

with the assumption that

$$\kappa = \frac{\alpha_u \alpha_{d'}}{\alpha_{u'} \alpha_d} = 1 \; . \tag{6.8}$$

Eq. (6.8) only implies that if the acceptance changes with time, it changes in the same way for both target cells. The fluxes cancel in κ since both target cells are subject to the same flux ($\Phi_u = \Phi_d$ and $\Phi_{u'} = \Phi_{d'}$). The number of target particles n_t and the unpolarized cross section σ_t drop out, because they are the same before and after a field reversal ($n_t = n_{t'}$ and $\sigma_t = \sigma_{t'}$, $t = u, d$). For a more detailed discussion see App. C. A possible deviation of κ from 1 is a source of systematic error. If the factors $<\beta_t>$ are known, eq. (6.7) provides a quadratic equation in $A_S \equiv \Delta G/G$.

This can be formulated in a different way. With 4 equations:

$$\begin{aligned} N_t &= \alpha_t (1- <\beta_t> A_S) & (6.9) \\ & \quad \text{with } t = u, d, u', d' \; , & (6.10) \end{aligned}$$

one can extract 4 unknowns:

$$A_S, \alpha_u, \alpha_d, \alpha_{u'} \; , \tag{6.11}$$

($\alpha_{d'}$ is fixed through the condition eq. (6.8)).

We now turn to the determination of the factor $<\beta>$. Its value is taken as the average over the event sample:

$$<\beta> = \frac{\sum_{i=1}^{N} \beta_i}{N} \; . \tag{6.12}$$

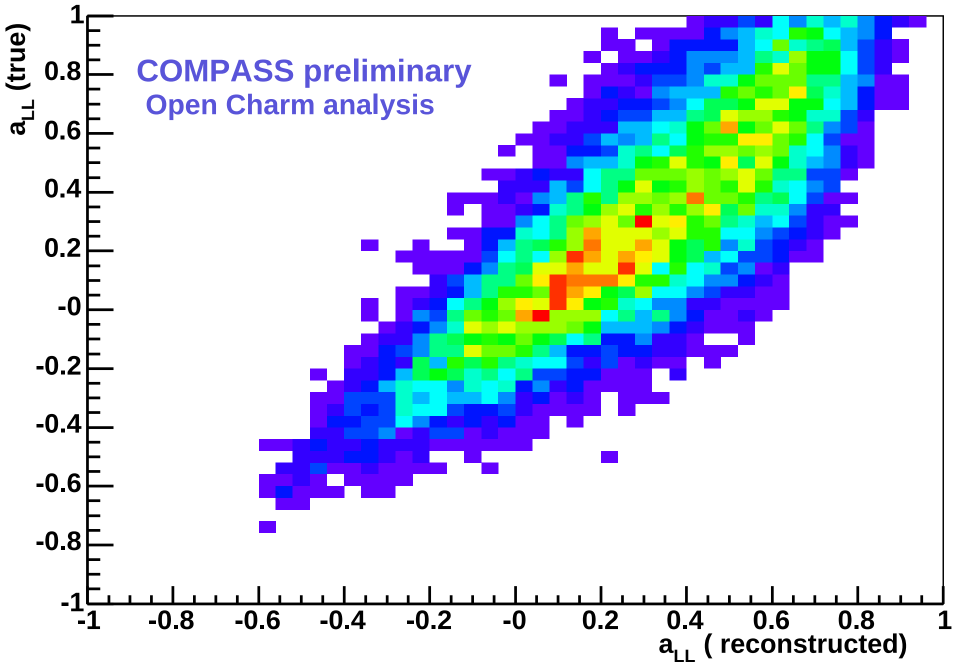

Figure 6.4: The true vs. reconstructed a_{LL}.

The difficulty in calculating $<\beta>$ is that not all factors are known event by event. The target and beam polarization and the dilution factor f are known event by event. The partonic asymmetry a_{LL} is not, because it depends on the parton kinematics which is not directly accessible from the kinematics of the reconstructed particles. For the same reason the gluon momentum fraction x_g is not known event by event. Here one uses a neural network parameterization of a_{LL} as a function of known kinematic variables y, p_T and z_D obtained with the help of an AROMA-MC simulation([21],[19] section 6.3.2). Fig. 6.4 shows the true analyzing power vs. the parameterized one. The correlation reaches 82%. Fig. 6.5 shows a comparison of data and MC for the three variables y, p_T and z_D. The MC contains only signal events. In the data the background was subtracted using the sidebands in the mass spectra. The agreement is satisfactory, so that one can trust the MC simulation for the parameterization of a_{LL}.

The fraction of signal events $\sigma_{PGF}/(\sigma_{PGF} + \sigma_B)$ is known from Figs. 6.1 and 6.2 only as a function of the reconstructed D^0 mass. In principle it would

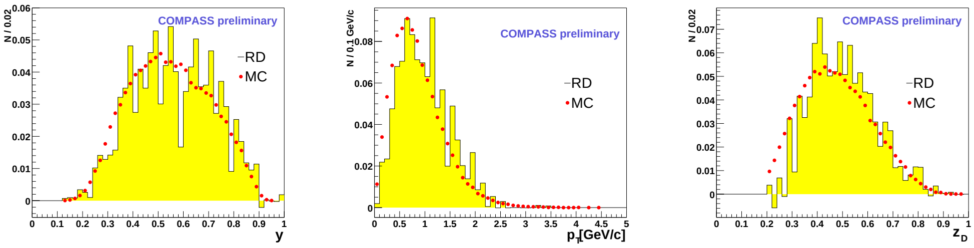

Figure 6.5: Data to MC comparison for $y, p_T\ z_D$. The MC contains only signal events. In the data the background was subtracted using the sidebands in the mass spectra.

be possible to produce these mass distributions in bins of other kinematic variables like y, p_T and z, but the available statistics does not allow a binning in all these variables. To solve this problem the ratio $\sigma_{PGF}/(\sigma_{PGF}+\sigma_B)$ is determined in bins of fP_Ba_{LL} as shown in Fig. 6.6 for the D^* case, i.e. for an event in a given bin of fP_Ba_{LL} the signal fraction is taken from a fit to the corresponding histogram in Fig. 6.6. Within one target cell the parameters $\sigma_1, m_1, \sigma_2, m_2$ and s in eq. (6.4) are the same for the different fP_Ba_{LL} bins, i.e. there is one fit performed for all the five histograms in one target cell. A similar method is applied for the D^0 case. Unfortunately the most favorable signal to background ratio is reached in the first bin where a_{LL} is close to 0. Ignoring this correlation would be equivalent to calculate

$$< P_B P_T f a_{LL} >< \frac{\sigma_{PGF}}{\sigma_{PGF}+\sigma_B} >$$

rather than the correct factor

$$< \beta >=< P_B P_T f a_{LL} \frac{\sigma_{PGF}}{\sigma_{PGF}+\sigma_B} > \ .$$

Extracting $\Delta G/G$ with smallest statistical error.

Another issue to consider is the way to extract $\Delta G/G$ with the smallest possible statistical error. From eq. (6.7) one finds for the statistical error or

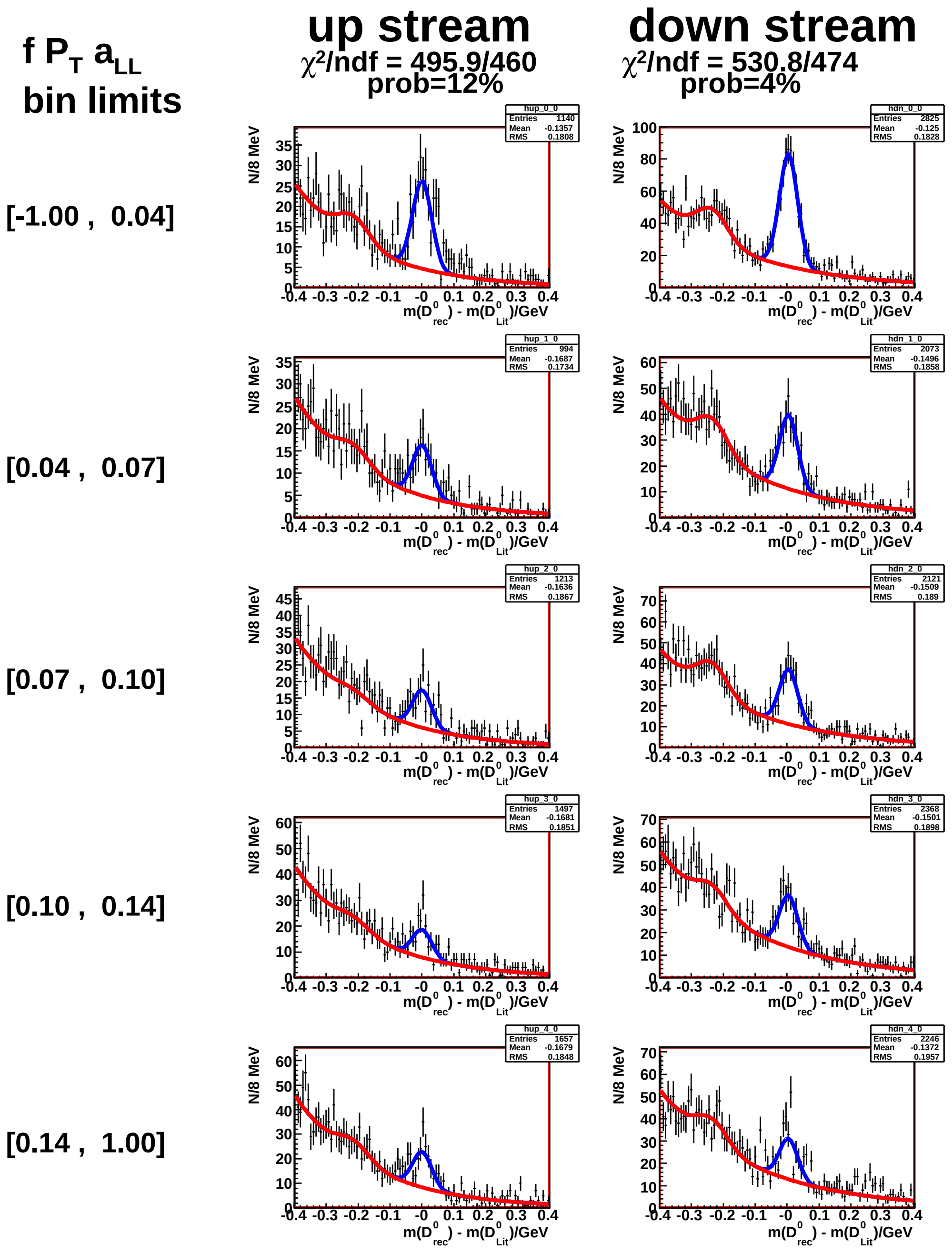

Figure 6.6: Invariant mass spectrum of $K^-\pi^+$ and $K^+\pi^-$ pairs of 2004 data with cuts given in the third column (D^*) in Tab. 6.1 for both target cells and different bins in $P_B f a_{LL}$. Within one target cell the parameters $\sigma_1, m_1, \sigma_2, m_2$ and s in eq. (6.4) are the same for the different $f P_B a_{LL}$ bins, i.e. there is one fit performed for all the five histograms in one target cell. The corresponding χ^2 for each target cell is given in the plot. The fits to these spectra are used in the analysis to evaluate $\frac{\sigma_{PGF}}{\sigma_{PGF}+\sigma_B}$.

the figure of merit (FOM):

$$\begin{aligned} \text{FOM} = \frac{1}{\sigma^2_{A_S}} &= \left(\frac{\partial A_S}{\partial \delta}\right)^{-2} (\sigma_\delta)^{-2} \\ &= 16 < \beta >^2 \frac{N_{tot}}{16} \\ &= < \beta >^2 N_{tot} \end{aligned} \tag{6.13}$$

where $N_{tot} = N_u + N_d + N_{u'} + N_{d'}$ is the total number of events. To simplify the discussion we assumed in eq. (6.13)

$$N_u \approx N_d \approx N_{u'} \approx N_{d'}$$

and

$$< \beta > := < \beta_u > \approx < \beta_{d'} > \approx - < \beta_{u'} > \approx - < \beta_d > \ .$$

An expression for the FOM dropping these assumptions can easily be derived, but is irrelevant for the following discussion.

In section 4 we saw that a_{LL} has positive and negative values. Thus $< \beta >$ may be close to 0 and the FOM even vanishes for the case $< \beta >= 0$! One can of course divide the event sample in bins of β and extract $\Delta G/G$ separately in every bin. Since these measurements are independent the FOM is now given by

$$\text{FOM} = \Sigma_{i=1}^{N_{bin}} \beta_i^2 N_i \tag{6.14}$$

or in the limit of an infinite number of bins:

$$\text{FOM} = < \beta^2 > N_{tot} \, , \tag{6.15}$$

which results in a gain in the FOM of

$$\frac{< \beta^2 >}{< \beta >^2} \tag{6.16}$$

with respect to the case without binning.

Dividing the sample in bins is inconvenient because of possible problems with low or 0 number of events in certain bins. App. D shows that one reaches the same FOM by weighing every event with an appropriate factor. This optimal weight factor turns out to be just the diluting factor β. The target polarization P_T is not included in the weight because it would lead to an increase in the systematic error, as explained in App. B.

In the weighting procedure, instead of using the event rates

$$N_u, N_d, N_{u'} \quad \text{and} \quad N_{d'} \;,$$

one considers the sum over event weights

$$p_u = \Sigma_{i=1}^{N_u} w_i,\; p_d = \Sigma_{i=1}^{N_d} w_i,\; p_{u'} = \Sigma_{i=1}^{N_{u'}} w_i \quad \text{and} \quad p_{d'} = \Sigma_{i=1}^{N_{d'}} w_i \tag{6.17}$$

with $w_i = P_B f a_{LL} \frac{\sigma_{PGF}}{\sigma_{PGF}+\sigma_B}$ and proceeds in the same way as in the unweighted case, i.e. one calculates the double ratio

$$\delta = \frac{p_u p_{d'}}{p_{u'} p_d} = \frac{\alpha_u \alpha_{d'}}{\alpha_{u'} \alpha_d} \frac{(1- <\beta_u>_w A_S)(1- <\beta_{d'}>_w A_S)}{(1- <\beta_{u'}>_w A_S)(1- <\beta_d>_w A_S)} \tag{6.18}$$

with

$$\begin{aligned} <\beta_t>_w &= \frac{\int \beta_t w \mathrm{d}^n x}{\int w \mathrm{d}^n x} \approx \frac{\sum \beta_t w}{\sum w} \;, \\ \alpha_t &= \int w \, a_t \, \Phi_t \, n_t \, \sigma_t \, \mathrm{d}^n x \\ & \quad t = u, d, u', d' \;. \end{aligned}$$

In this case one finds for the FOM:

$$\begin{aligned} \mathrm{FOM} = \frac{1}{\sigma^2_{A_S}} &= \left(\frac{\partial A_S}{\partial \delta}\right)^{-2} (\sigma_\delta)^{-2} \\ &= 16 < \beta w >^2_w \frac{<w>^2}{16 <w^2>} N_{tot} \\ &\overset{w \equiv \beta}{=} < \beta^2 > N_{tot} \,. \end{aligned} \tag{6.19}$$

Thus with the choice $w = \beta$, the FOM is the same as for the case of dividing the sample in an infinite number of bins. App. D even shows that this choice of weight corresponds to the minimal statistical error one can reach.

Taking into consideration the background asymmetry A_B

Up to now the background asymmetry A_B has been neglected. One could correct for it by taking events in the sidebands of the mass distributions in Fig. 6.1 and 6.2. This is not the most efficient solution as will be shown in the following. In the case of a non vanishing background asymmetry eq. (B.24) is extended to

$$N = \tilde{\alpha}\,(1 - \beta_S A_S - \beta_S A_B) \tag{6.20}$$

$$\text{with} \quad \tilde{\alpha} = a\Phi n\sigma\,, \tag{6.21}$$

$$\beta_S = P_B P_T f a_{LL} \frac{\sigma_{PGF}}{\sigma_{PGF} + \sigma_B}\,, \tag{6.22}$$

$$\beta_B = P_B P_T f a_{LL}^B \frac{\sigma_B}{\sigma_{PGF} + \sigma_B}\,. \tag{6.23}$$

Now one introduces two weight factors, one for the signal,

$$w_S = P_B f a_{LL} \frac{\sigma_{PGF}}{\sigma_{PGF} + \sigma_B}\ ,$$

and one for the background,

$$w_B = P_B f a_{LL}^B \frac{\sigma_B}{\sigma_{PGF} + \sigma_B}\ .$$

The expectation value of $\sum_{i=1}^{N_t} w_{S,B}^i$ is given by multiplying eq. (6.20) with the weight factor and integrating over $\mathrm{d}^n x$. This leads to the following 8 equations:

$$\sum_{i=1}^{N_t} w_S^i = \alpha_{t,S}\ (1 + <\beta_{t,S}>_{w_S} A_S + <\beta_{t,B}>_{w_S} A_B)\ ,$$

$$\sum_{i=1}^{N_t} w_B^i = \alpha_{t,B}\ (1 + <\beta_{t,S}>_{w_B} A_S + <\beta_{t,B}>_{w_B} A_B)\ ,$$

with

$$\alpha_{t,C} = \int \tilde{\alpha}_t w_C \mathrm{d}^n x\ , \tag{6.24}$$

$$<\beta_{t,C}>_{w_{C'}} = \frac{\int \beta_C w_{C'} \alpha_t \mathrm{d}^n x}{\int w_C \alpha_t \mathrm{d}^n x}\ , \tag{6.25}$$

$$t = u, d, u', d'\ , \quad C = S, B\ , \quad C' = S, B\ .$$

With these 8 equations the 8 parameters

$$A_S, A_B, \alpha_{u,S}, \alpha_{d,S}, \alpha_{u',S}, \alpha_{u,B}, \alpha_{d,B} \quad \text{and} \quad \alpha_{u',B}$$

can be extracted. This method allows thus the simultaneous extraction of A_S and A_B.

$\alpha_{d',S}$ and $\alpha_{d',B}$ are fixed through the acceptance conditions

$$\frac{\alpha_{u,S}\,\alpha_{d',S}}{\alpha_{u',S}\,\alpha_{d,S}} = 1 , \qquad \frac{\alpha_{u,B}\,\alpha_{d',B}}{\alpha_{u',B}\,\alpha_{d,B}} = 1 . \tag{6.26}$$

One can try to reduce the number of unknowns further, by assuming that

$$\frac{\alpha_{u,S}}{\alpha_{u,B}} = \frac{\alpha_{u',S}}{\alpha_{u',B}} . \tag{6.27}$$

This will reduce the number of unknowns from 8 to 7 (Because of eq. (6.26) this implies also that $\alpha_{d,S}/\alpha_{d,B} = \alpha_{d',S}/\alpha_{d',B}$). This assumption is weaker than the assumption in eq. (6.26) since it only demands that if the acceptance changes, it changes in the same way for the signal and the background.

Since the system is over-constrained (8 equations for 7 unknowns) it allows even to verify the underlying assumptions by looking at the χ^2 distribution. More details are presented in App. E.

Fig. 6.7 shows the results obtained for $A_S \equiv \Delta G/G$ and A_B for the two decay channels and the different years of data taking. With the method described above $\Delta G/G$ is extracted with the highest statistical accuracy. As explained after eq. (6.19) the same results can in principle be obtained by binning the event sample. This will be discussed in the following. Fig. 6.8 shows the muon-nucleon asymmetry of the open charm events in four bins of a_{LL} for the two decay channels. The muon-nucleon asymmetry is obtained by excluding a_{LL} from the weighting factor. According to eq. (B.14):

$$A^{\mu N} = < a_{LL} > \frac{\Delta G}{G} ,$$

$\Delta G/G$ is given by the slope of a straight line going through the origin of the coordinate system, assuming a constant $\Delta G/G$. At the present accuracy of the data the assumption that $\Delta G/G$ is constant seems to be justified. In Tab. 6.2 the results obtained by this method are compared to the results obtained by including a_{LL} in the weight.

Systematic Errors

The relative errors of the beam, target polarization and the dilution factor are 5% for each of these factors. Varying the charm mass m_c in the range

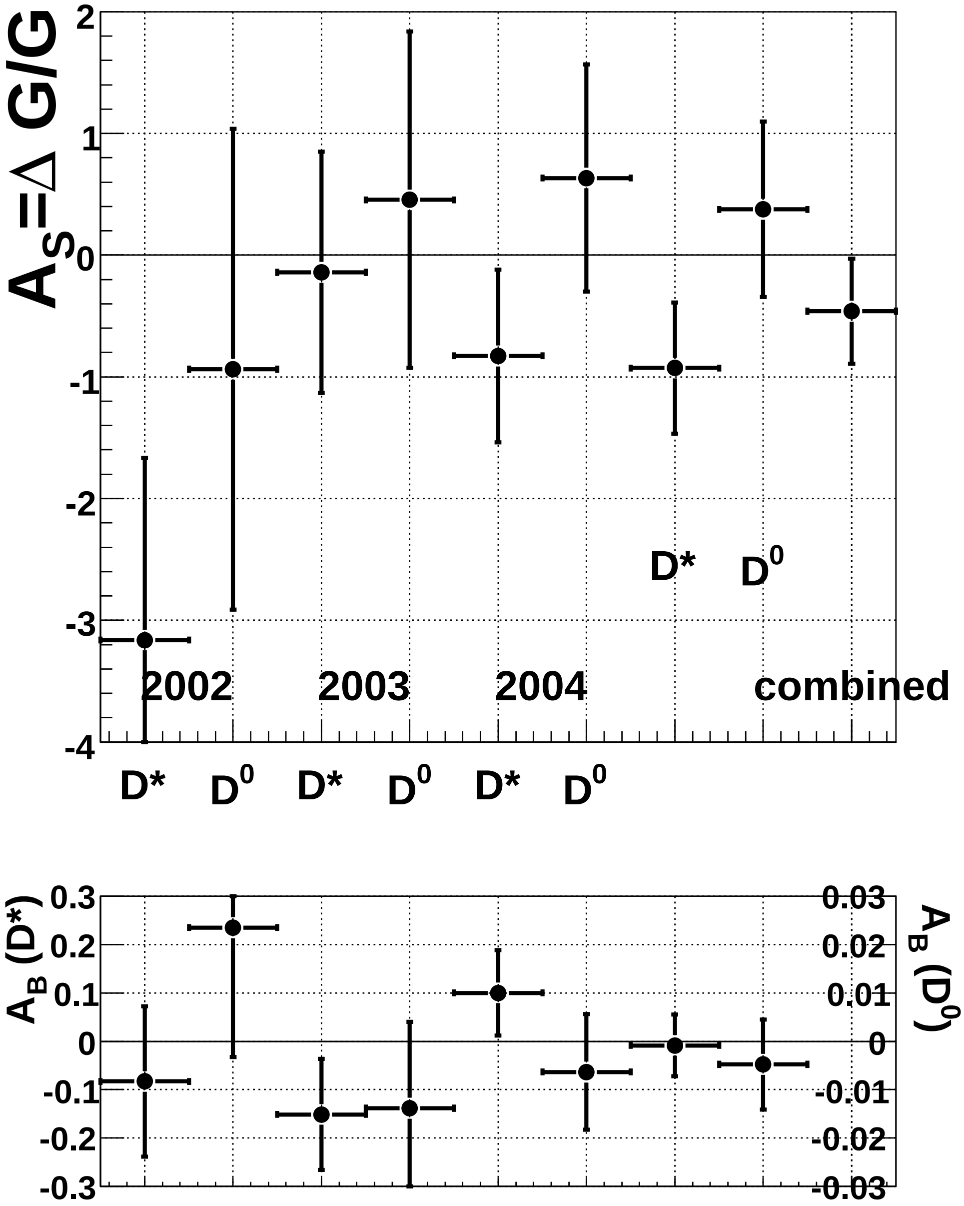

Figure 6.7: Results for $A_S \equiv \Delta G/G$ and A_B for the two decay channels and the different years of data taking. The horizontal axis is the same for both histograms. Note that in the lower histogram the left vertical scale is for the D^* background asymmetry and the right scale for the D^0 background asymmetry.

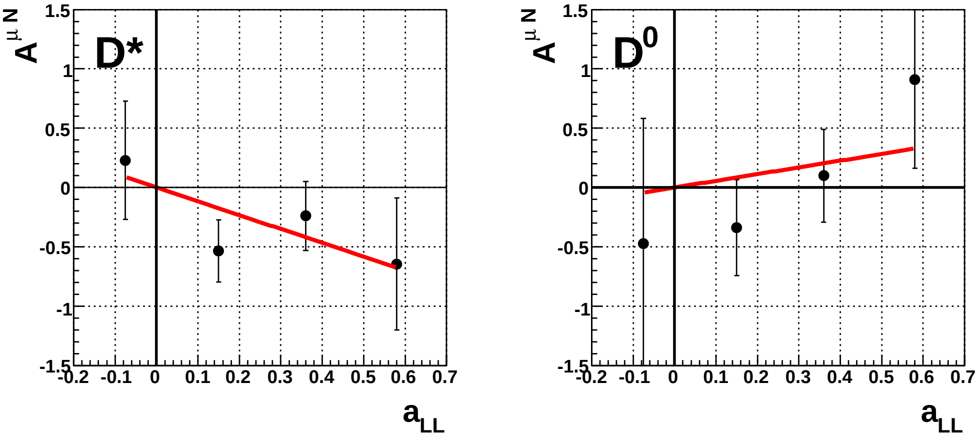

Figure 6.8: The muon-nucleon asymmetry of the open charm events as a function of a_{LL}. The lines are fits to the data using eq. (B.14). The slope of the lines is $\Delta G/G$.

method	D^*	D^0
a_{LL} bins	-1.17 ± 0.58	0.57 ± 0.79
a_{LL} in weight	-0.93 ± 0.54	0.38 ± 0.72
difference	-0.24 ± 0.21	0.19 ± 0.33

Table 6.2: Comparison of results on $\Delta G/G$ obtained by analyzing the data in bins of a_{LL} and including a_{LL} in the weight. The error on the difference is given by: $\sigma^2_{diff} = \sigma^2_{a_{LL}\,\mathrm{bins}} - \sigma^2_{a_{LL}\,\mathrm{in\ weight}}$ [22].

source	contribution
P_B	5%
P_T	5%
f	5%
a_{LL}	0.05
$\frac{\sigma_{PGF}}{(\sigma_{PGF}+\sigma_B)}$	0.09
binning in fPa_{LL}	0.04
$\kappa \neq 1$	0.10
total (for $\Delta G/G = -0.46$)	0.15

Table 6.3: Contribution to the systematic error of $\Delta G/G$.

1400–1600 GeV results in a change of 0.05 for $\Delta G/G$ due to a different a_{LL}. Trying different fitting procedures to describe the mass spectra, used to determine the factor $\sigma_{PGF}/(\sigma_{PGF} + \sigma_B)$, results in a contribution of 0.09. Varying the binning in fP_Ba_{LL} yields a contribution of 0.04.

In addition to these contributions there is another one due to false asymmetries by a possible violation of the relation (6.26). This was estimated by looking at the deviation of a result obtained in one configuration, $(\Delta G/G)_i$, from the average result ,$<\Delta G/G>$, divided by the statistical error σ_i:

$$\frac{(\Delta G/G)_i - <\Delta G/G>}{\sigma_i} .$$

This distribution is centered around 0 with an RMS of 1, if relation (6.26) is fulfilled. No deviation from 1 was observed. As an upper limit one finds a contribution of 0.10 to the systematic error.

Adding all contributions listed in Tab. 6.3 in quadrature results in a total systematic error of 0.15. Note that all systematic studies were performed independently for the two decay channels. The various contributions were found to be very similar for both decay channels, such that only one value is given in Tab. 6.3.

The final result

It remains to clarify at which momentum fraction x_g and scale μ the gluon polarization is measured. As for a_{LL}, a MC simulation is used to determine

$< x_g >$. One finds a value of $< x_g >= 0.15$ with an RMS of 0.08. The scale is approximately given by $\mu^2 = 4(m_c^2 + p_T^2) \approx 13$ GeV^2.

The combined value (both decay channels, all years) is

$$\begin{aligned} \frac{\Delta G}{G} &= -0.46 \pm 0.43 \pm 0.15 \ , \\ &\ \text{at} \quad < x_g >= 0.15 \\ &\ \text{and} \quad \mu^2 = 13\text{GeV}^2 \ . \end{aligned} \tag{6.28}$$

6.2 High p_T analysis

The event sample with two hadrons of large transverse momentum is divided into two subsamples, $Q^2 < 1\text{GeV}^2$ and $Q^2 > 1$ GeV^2. The reason is that different Monte Carlo generators are used to estimate the various background contributions. For the events with $Q^2 < 1$ GeV^2 the generator PYTHIA [23] and for events $Q^2 > 1$ GeV^2 the generator LEPTO [24] is used. Events with $Q^2 < 1\text{GeV}^2$ correspond to 90% of the total sample. Concerning the scattered muon, the event selection is similar to the open charm analysis.

6.2.1 High p_T, $Q^2 < 1$ GeV^2

For this sample the cuts listed in Tab. 6.4 were applied. They were optimized to find a good balance between clear tagging of the PGF process (tight cuts) and high statistics (loose cuts). These cuts result in contributions R for the various partonic subprocesses shown in Fig. 6.9. The first three are the PGF, the QCD Compton (QCDC) and the LO process. The virtual photon can also fluctuate in a hadron and a parton of the resolved photon interacts with a parton in the nucleon. These are the next three contributions shown in the figure. Finally the low p_T contribution reflects resolved photon events where no hard scale is present.

The raw asymmetry A^{raw} is related to $\Delta G/G$ in the following way:

$$A^{raw} = f\, P_B\, P_T\, (R_{PGF}\, a_{LL}^{PGF}\, \frac{\Delta G}{G} + A_B) \ . \tag{6.29}$$

$Q^2 < 1 GeV^2$
$0.3 < y < 0.9$
$m(h_1, h_2) > 1.5$ GeV
$x_F > 0.1$
$p_T^{h_1}, p_T^{h_2} > 0.7$ GeV
$(p_T^{h_1})^2 + (p_T^{h_2})^2 > 2.5$ GeV^2

Table 6.4: Cuts used to enhance the PGF sample in the $Q^2 < 1$ GeV^2 sample.

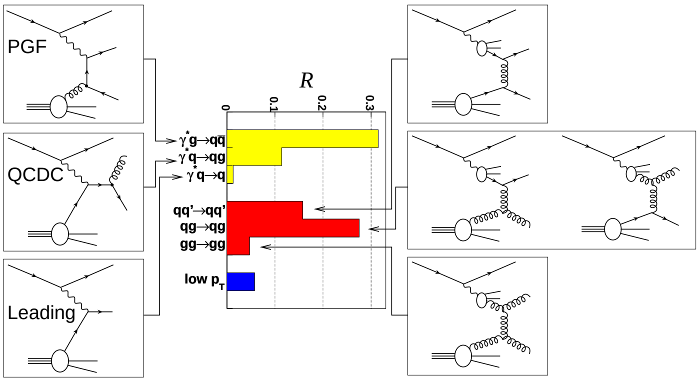

Figure 6.9: The various partonic subprocesses contributing to the cross section for the cuts listed in Tab. 6.4.

The background asymmetry receives the following contributions:

$$\begin{aligned} A_B &= R_{QCDC}\, a_{LL}^{QCDC} A^{QCDC} \\ &+ R_{LO}\, a_{LL}^{LO} A^{LO} \\ &+ R_{\mathrm{low}_{p_T}}\, a_{LL}^{\mathrm{low}_{p_T}} A^{\mathrm{low}_{p_T}} \\ &+ \Sigma_{f,f'=u,d,s,\bar{u},\bar{d},\bar{s},G}\, R_{ff'} a_{LL}^{ff'} \frac{\Delta f}{f} \frac{\Delta f'}{f'} \,. \end{aligned} \tag{6.30}$$

The factors R designate the fraction of the corresponding process to the cross section. The partonic asymmetries are denoted by a_{LL}. R_{PGF} is approximately 30% and $a_{LL}^{PGF} \approx -0.6$ at $y = 0.5$ (see Fig. 4.3).

The contribution of the LO and low p_T process amounts only to about 7%. Moreover their contribution is multiplied by an asymmetry which is known to be very small in the kinematic region considered [25, 26]. Therefore these two contributions are neglected. The QCDC contribution can be estimated from the measured inclusive deuteron asymmetry A_1^d. To evaluate the resolved photon contributions, one has to know the polarization of the partons in a resolved photon. Unfortunately these are unknown and only limits can be given [27], which leads to a contribution to the systematic error.

Systematic Error

In this analysis the fraction of signal events R_{PGF} must be extracted from the generated MC sample. It is thus mandatory to find a good agreement between data and MC. The level of agreement is shown in Fig. 6.10. Several PYTHIA parameters relevant to the amount of transverse momentum acquired by hadrons were varied in a range in which the agreement between data and MC remains satisfactory. The resulting variation of $\Delta G/G$ gives a contribution to the systematic error of 0.035. Higher order QCD effects were estimated by varying the factorization and renormalization scale by a factor of 2 resulting in a contribution of 0.008. The uncertainty in the polarized parton distribution of the photon results in a contribution of 0.015. Together with other experimental systematic error sources, similar to the open charm analysis, the total systematic error is 0.055.

The scale is approximately given by $\mu^2 \approx (p_T^{h_1})^2 + (p_T^{h_2})^2 \approx 3$ GeV^2. From the MC simulation the average gluon momentum fraction was determined to

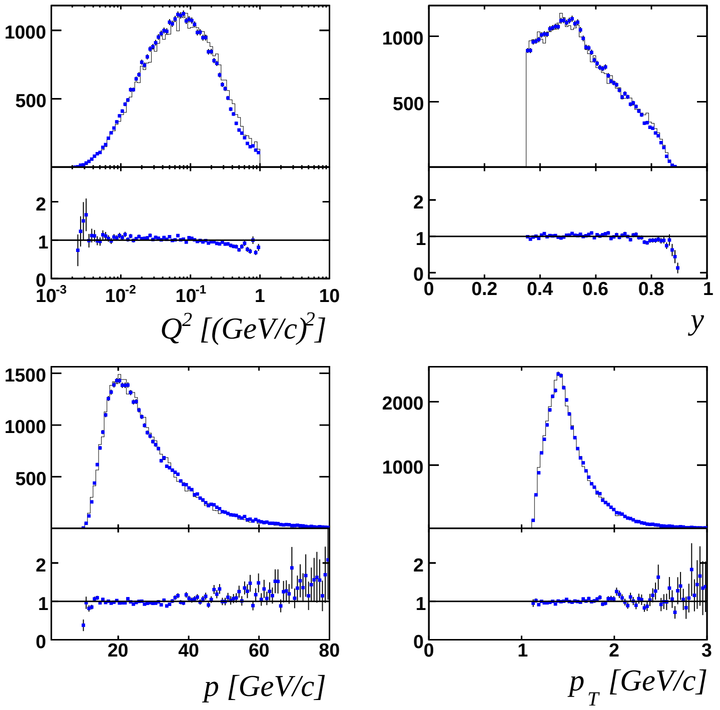

Figure 6.10: Data vs. MC comparison for Q^2,y,p and p_T. The upper part of each plot shows the simulated (line) and the data (points) normalized to the number of events. The lower part shows the ratio data/MC.

$m(h_1, h_2)$	$>$	1.5 GeV
x_F	$>$	0.1
z	$>$	0.1
p_T	$>$	0.7 GeV
$(p_T^{h_1})^2 + (p_T^{h_2})^2$	$>$	2.5 GeV^2

Table 6.5: Cuts used to enhance the PGF sample in the $Q^2 > 1\text{GeV}^2$ analysis.

be $< x_g >= 0.085$ with an RMS of 0.05. The final result is

$$\begin{aligned} \frac{\Delta G}{G} &= 0.016 \pm 0.058 \pm 0.055 \;, \\ &\text{at} \quad < x_g >= 0.085 \\ &\text{and} \quad \mu^2 = 3\,\text{GeV}^2 \;. \end{aligned} \tag{6.31}$$

A more detailed description of this analysis can be found in [28]. An analysis including only the 2002 and 2003 data is published in [26].

6.2.2 High p_T, $Q^2 > 1$ GeV^2

For events with $Q^2 > 1$ GeV^2 the contribution of resolved photons can be neglected. Here the cross section is described by three processes:

- Leading order (31%)
- QCD Compton (32.5%)
- Photon Gluon Fusion (36.5%)

For this analysis the event generator LEPTO [24] was used to estimate the contributions of these three subprocesses to the cross section. After optimizing the cuts given in Tab. 6.5 the event fractions given in parentheses are obtained. The level of agreement between data and MC can be judged in Fig. 6.11. The total systematic error is 0.06. It contains contributions from experimental systematic errors and from the MC generator.

The final result is:

$$\begin{aligned} \frac{\Delta G}{G} &= 0.06 \pm 0.31 \;\pm 0.06 \;, \\ &\text{at} \quad < x_g >= 0.13 \\ &\text{and} \quad \mu^2 = 2.4\,\text{GeV}^2 \;. \end{aligned} \tag{6.32}$$

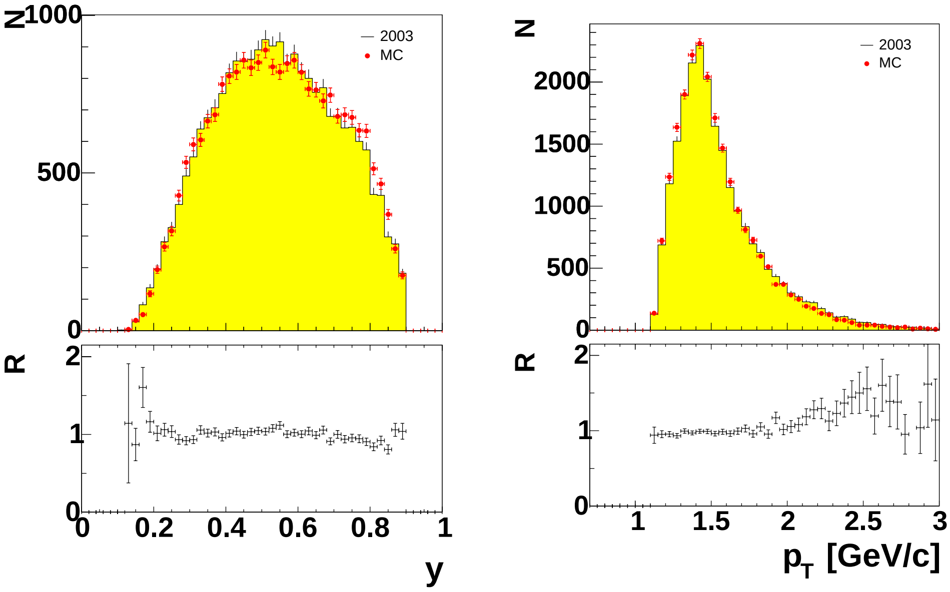

Figure 6.11: Data to MC comparison for one inclusive variable, y, and one semi-inclusive variable, the transverse momentum of the hadron with the largest p_T[29].

This result includes only data from 2002 and 2003. The analysis of the 2004 data is still ongoing. A more detailed description of this analysis can be found in [29].

6.3 Summary of Results on $\Delta G/G$

Fig. 6.12 and Tab. 6.6 show the results obtained by the COMPASS collaboration and other experiments and compare them with predictions obtained from NLO analyses of inclusive data. The direct measurements are incompatible with parameterizations predicting a large first moment of $\Delta G = 2-3$.

Fig. 6.13 shows results from the PHENIX and STAR collaboration at the polarized proton-proton collider RHIC. These results confirm that scenarios with a large ΔG are ruled out.

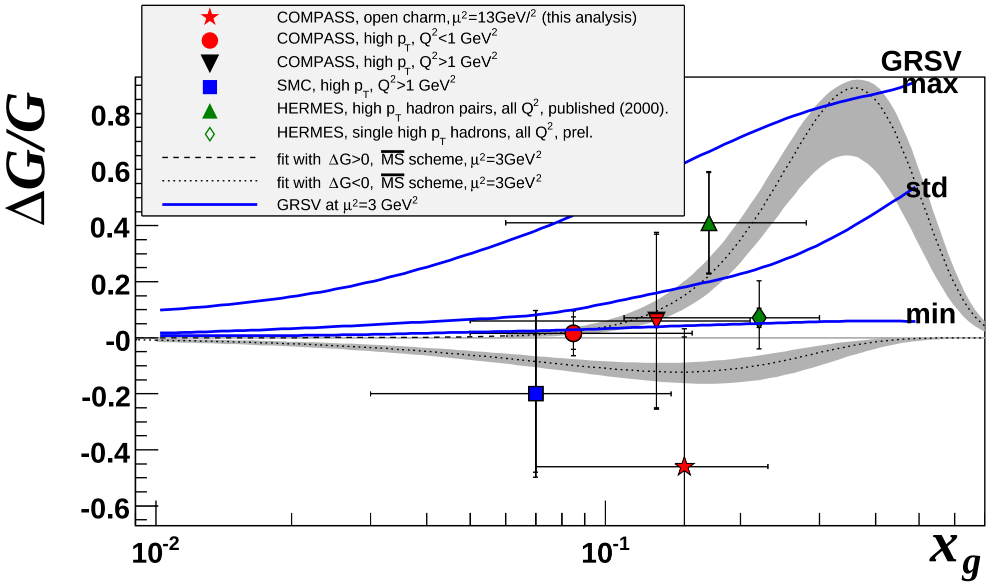

Figure 6.12: Results on $\Delta G/G$ from different experiments. The two dotted curves are results from the COMPASS NLO fits to inclusive asymmetries [12]. The corresponding first moments are 0.26 and -0.31 at $\mu = 3\text{GeV}^2$. The three solid curves labeled max, std and min are parameterizations from GRSV [30]. They correspond to first moments at $\mu = 3\text{GeV}^2$ of 2.5, 0.6, 0.2 respectively.

Experiment	Method	$\Delta G/G \pm$ stat. err $\pm$ sys. err.	scale μ/GeV^2	$< x_g >$	ref.
COMPASS	hadron pairs, $Q^2 < 1$ GeV^2	$0.016 \pm 0.058 \pm 0.055^{1)}$	3	0.085	[33]
COMPASS	hadron pairs, $Q^2 > 1$ GeV^2	$0.06 \pm 0.31 \pm 0.06^{1)}$	2.4	0.13	[33]
COMPASS	open charm	$-0.46 \pm 0.43 \pm 0.15$	13	0.15	
HERMES	hadron pairs	$0.41 \pm 0.18 \pm 0.03^{2)}$	2	0.17	[34]
HERMES	single hadrons	$0.071 \pm 0.034^{+0.105}_{-0.127}$	1.35	0.22	[35]
SMC	hadron pairs, $Q^2 > 1$ GeV^2	$-0.20 \pm 0.28 \pm 0.10$	3	0.07	[25]

Table 6.6: Results on $\frac{\Delta G}{G}$ from various experiments. $^{1)}$ These results do not include the correction for the D-state probability in the deuteron mentioned in section 5.3. $^{2)}$ Only the experimental systematic error is given.

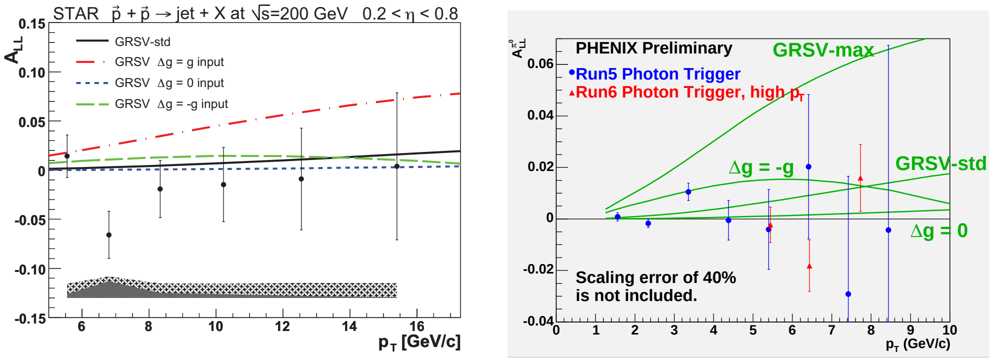

Figure 6.13: The double spin asymmetry A_{LL} as a function of p_T for inclusive jet production from the STAR experiment [31] (left) and for inclusive π^0 production from the PHENIX experiment [32] (right). The parameterizations [30] labeled $\Delta G = -G, \Delta G = 0$ and $\Delta G = G$ correspond to gluon distributions of $\Delta G = -G, 0, G$ at an input scale of $Q^2 = 0.4$ GeV^2. The parameterizations labeled GRSV-max and GRSV-std correspond to first moments of 2.5 and 0.6 at a scale $\mu = 3\text{GeV}^2$.

Chapter 7

Summary & Outlook

This work describes the measurement of the gluon polarization in the nucleon performed by the COMPASS collaboration. The motivation for such a measurement is the fact that a large first moment of the polarized gluon distribution $\Delta G = \int_0^1 \Delta G(x_g)\,dx_g \approx 2 - 3$ would reconcile predictions for the quark spin contribution from quark models and deep inelastic scattering. COMPASS data show that $\Delta G/G$ is small at $x_g \approx 0.1$ and not compatible with parameterizations that predict large values for ΔG. These direct measurements only determine $\Delta G/G$ in a limited momentum range. NLO QCD analysis, which provide an indirect measurement of the first moment, confirm a small value of ΔG. Although all the results presented here are compatible with $\Delta G = 0$, with the present precision of the experimental data, it is still possible that the spin of the gluons is responsible for 100% of the nucleon spin, i.e. $\Delta G = \frac{1}{2}$. Thus the question about the origin of the nucleon spin remains open.

In the near future new data from COMPASS and the *pp* collider RHIC will further reduce the uncertainty on $\Delta G/G$. In the long term a new electron proton collider like eRHIC[36] would provide an ideal tool for a precise determination of the shape of $\Delta G(\mathbf{x_g})$. Finally, deep virtual Compton scattering (DVCS) was proposed [37] to measure the contribution of the orbital angular momentum to the nucleon spin.

Appendix A

D-state probability in the Deuteron wave function

The deuteron wave function is given by:

$$|d>= \alpha_S|S> +\alpha_D|D> \tag{A.1}$$

with $\alpha_D = 0.05$ [16] and $\alpha_S^2 + \alpha_D^2 = 1$.

For a deuteron with total angular momentum $J = 1$ and $M_J = 1$ the $|S>$ and the $|D>$ states are given in terms of the orbital angular momentum L and the spin S by:

$$\begin{aligned} |S> &= |0,0,1,1>= |L, M_L, S, M_S> \\ |D> &= <1,1|2,2,1,-1> |2,2,1,-1> \\ &+ <1,1|2,1,1,0> |2,1,1,0> \\ &+ <1,1|2,0,1,1> |2,0,1,1> \\ &= \sqrt{\frac{3}{5}}\,|2,2,1,-1> -\sqrt{\frac{3}{10}}\,|2,1,1,0> +\sqrt{\frac{1}{10}}\,|2,0,1,1>, \end{aligned}$$

where in the state vectors the quantum numbers are $|L, M_L, S, M_S>$ and in the Clebsch-Gordan coefficients they are $< J, M_J|L, M_L, S, M_S >$.

How large is the polarization of the two nucleons in the deuteron in the state $|J = 1, M_J = 1>$?

This polarization is given by:

$$\begin{aligned}< 1,1|\hat{S}_z|1,1 > &= \alpha_S^2 \cdot 1 + \alpha_D^2 \left(\frac{3}{5} \cdot (-1) + \frac{3}{10} \cdot 0 + \frac{1}{10} \cdot 1 \right) \\ &= 1 - \alpha_D^2 + \alpha_D^2 \left(-\frac{6}{10} + \frac{1}{10} \right) = \left(1 - \frac{3}{2}\alpha_D^2 \right) ,\end{aligned}$$

i.e. in a totally polarized deuteron the nucleons are only polarized to

$$\left(1 - \frac{3}{2}\alpha_D^2 \right) = 92.5\%$$

for a D-state probability of $\omega_D = \alpha_D^2 = 0.05$.

Appendix B

Relation between counting rate and asymmetry

The number of events can be written as:

$$N = a\Phi(\Sigma_A n_A \sigma_A + n_P^{\uparrow\uparrow}\sigma_P^{\uparrow\uparrow} + n_P^{\uparrow\downarrow}\sigma_P^{\uparrow\downarrow})\,. \tag{B.1}$$

The variables used in eq. (B.1) are explained in Tab. B.1.

The product of the target and beam polarization can be expressed in terms of $n_P^{\uparrow\uparrow}$ and $n_P^{\uparrow\downarrow}$:

$$P_T P_B = \frac{n_P^{\uparrow\uparrow} - n_P^{\uparrow\downarrow}}{n_P^{\uparrow\uparrow} + n_P^{\uparrow\downarrow}}\,. \tag{B.2}$$

Note that only the relative orientation between beam and target spin matters.

Replacing

$$n_P^{\uparrow\uparrow} = \frac{1 + P_T P_B}{2} n_P \quad \text{and} \quad n_P^{\uparrow\downarrow} = \frac{1 - P_T P_B}{2} n_P \tag{B.3}$$

in eq. (B.1) yields

$$\begin{aligned} N &= a\Phi\left[\Sigma_A n_A \sigma_A + n_p\left(\frac{1 + P_B P_T}{2}\,\sigma_p^{\uparrow\uparrow} + \frac{1 - P_B P_T}{2}\,\sigma_p^{\uparrow\downarrow}\right)\right] \\ &= a\Phi\left[\Sigma_A n_A \sigma_A + n_p\left(\frac{\sigma_P^{\uparrow\downarrow} + \sigma_P^{\uparrow\uparrow}}{2} - P_B P_T\,\frac{\sigma_P^{\uparrow\downarrow} - \sigma_P^{\uparrow\uparrow}}{2}\right)\right]\,. \end{aligned}$$

Variable	definition	meaning
a		acceptance
Φ		muon flux
n	$= n_P + \sum_A n_A$	total number of nuclei in target
$n_P^{\uparrow\uparrow} (n_P^{\uparrow\downarrow})$		number of nuclei with beam and target polarization parallel (anti-parallel).
$n_P, (n_A)$	$n_P = n_P^{\uparrow\uparrow} + n_P^{\uparrow\downarrow}$	number of polarizable (non-polarizable) nuclei
$\sigma_P, (\sigma_A)$		unpolarized cross section of polarizable (non-polarizable) nuclei
σ	$= \frac{n_P \sigma_P + \sum_A n_A \sigma_A}{n}$	average unpolarized cross section
f	$= \frac{n_P \sigma_P}{n_P \sigma_P + \sum_A n_A \sigma_A}$	dilution factor
$P_B, (P_T)$		beam (target) polarization
$A^{\mu N}$		Muon-Nucleon - asymmetry

Table B.1: Definition of the variables used in eq. (B.1).

We now introduce the muon-nucleon asymmetry, $A^{\mu N}$, and the unpolarized cross section σ_P

$$A^{\mu N} = \frac{\sigma_P^{\uparrow\downarrow} - \sigma_P^{\uparrow\uparrow}}{\sigma_P^{\uparrow\downarrow} + \sigma_P^{\uparrow\uparrow}} = \frac{\sigma_P^{\uparrow\downarrow} - \sigma_P^{\uparrow\uparrow}}{2\sigma_P} \,. \tag{B.4}$$

This leads to

$$N = a\Phi \left[\Sigma_A n_A \sigma_A + n_p \sigma_P \left(1 - P_B P_T A^{\mu N}\right)\right] \,. \tag{B.5}$$

Finally, the introduction of the dilution factor

$$f = \frac{n_P \sigma_P}{n_P \sigma_P + \Sigma_A n_A \sigma_A} \tag{B.6}$$

gives

$$N = a\Phi \left(\Sigma_A n_A \sigma_A + n_p \sigma_P\right) \left(1 - P_B P_T f A^{\mu N}\right) \tag{B.7}$$

with the definition of the average unpolarized cross section

$$\sigma = \frac{n_P \sigma_P + \Sigma_A n_A \sigma_A}{n_P + \Sigma_A n_A} = \frac{n_P \sigma_P + \Sigma_A n_A \sigma_A}{n} \tag{B.8}$$

one finally finds

$$N = a\Phi n \sigma \left(1 - P_B P_T f A^{\mu N}\right) \,. \tag{B.9}$$

We now turn to the relation between the muon-nucleon asymmetry, $A^{\mu N}$ and the parton distributions $\Delta q = q^{\uparrow} - q^{\downarrow}$ and $\Delta G = G^{\uparrow} - G^{\downarrow}$ we finally want to measure. The muon-nucleon cross section is related to the muon-gluon cross section in the following way:

$$\sigma^{\mu(\uparrow)N(\downarrow)} \propto \int \sigma^{\mu(\uparrow)G(\downarrow)} G^{\uparrow} + \sigma^{\mu(\uparrow)G(\uparrow)} G^{\downarrow} \, \mathrm{d}x_g \,, \tag{B.10}$$

$$\sigma^{\mu(\uparrow)N(\uparrow)} \propto \int \sigma^{\mu(\uparrow)G(\uparrow)} G^{\uparrow} + \sigma^{\mu(\uparrow)G(\downarrow)} G^{\downarrow} \, \mathrm{d}x_g \,. \tag{B.11}$$

The integral indicates that for a fixed event kinematics the gluon polarization is probed in a given range of the gluon momentum fraction x_g.

For the muon-nucleon asymmetry one finds

$$\begin{aligned} A^{\mu N} &= \frac{\sigma^{\mu(\uparrow)N(\downarrow)} - \sigma^{\mu(\uparrow)N(\uparrow)}}{\sigma^{\mu(\uparrow)N(\downarrow)} + \sigma^{\mu(\uparrow)N(\uparrow)}} \\ &= \frac{\int \left(\sigma^{\mu(\uparrow)G(\downarrow)} - \sigma^{\mu(\uparrow)G(\uparrow)}\right) (G^{\uparrow} - G^{\downarrow}) \mathrm{d}x_g}{\int \left(\sigma^{\mu(\uparrow)G(\downarrow)} + \sigma^{\mu(\uparrow)G(\uparrow)}\right) (G^{\uparrow} + G^{\downarrow}) \mathrm{d}x_g} \\ &= \frac{\int \frac{\Delta G}{G} \, a_{LL} \, \sigma^{\mu G} \, G \, \mathrm{d}x_g}{\int \sigma^{\mu G} \, G \, \mathrm{d}x_g} \end{aligned} \tag{B.12}$$

where the partonic asymmetry

$$a_{LL} = \frac{\sigma^{\mu(\uparrow)G(\downarrow)} - \sigma^{\mu(\uparrow)G(\uparrow)}}{\sigma^{\mu(\uparrow)G(\downarrow)} + \sigma^{\mu(\uparrow)G(\uparrow)}} \tag{B.13}$$

has been introduced. It depends on the photon-gluon kinematics. A leading order QCD expression can be found in [14].

To proceed further we assume that $\Delta G/G$ is constant [1] over the kinematic range considered.

and finally arrive at

$$A^{\mu N} \;=\; < a_{LL} > \frac{\Delta G}{G} \tag{B.14}$$

with

$$< a_{LL} >= \frac{\int a_{LL}\, \sigma^{\mu G}\, G \mathrm{d}x_g}{\int \sigma^{\mu G}\, G \mathrm{d}x_g}\;.$$

In the case of the inclusive asymmetry it is convenient to introduce the photon-nucleon asymmetry:

$$A^{\gamma N} = \frac{\sigma^T_{1/2} - \sigma^T_{3/2}}{\sigma^T_{1/2} + \sigma^T_{3/2}} \tag{B.15}$$

where $\sigma^T_{1/2}$ ($\sigma^T_{3/2}$) is the γ^*-nucleon absorption cross section for antiparallel (parallel) spin configuration of the photon-nucleon system. The relation between muon-nucleon and photon-nucleon cross section is given by

$$\sigma^{\mu(\uparrow)N(\downarrow)} \;\propto\; (P\sigma^T_{1/2} + (1-P)\sigma^T_{3/2} + \epsilon\,\sigma^L)\;, \tag{B.16}$$

$$\sigma^{\mu(\uparrow)N(\uparrow)} \;\propto\; ((1-P)\sigma^T_{1/2} + P\sigma^T_{3/2} + \epsilon\,\sigma^L) \tag{B.17}$$

where

$$\epsilon = \frac{2(1-y)}{2(1-y) + y^2} \tag{B.18}$$

---

[1] Actually, it can easily be shown that it is sufficient to assume a linear behavior: $\Delta G/G(x_g) = a(x_g - < x_g >) + b$. In this case $\Delta G/G$ is measured at a momentum fraction

$$< x_g >= \frac{\int x_g\, w\, a_{LL}\, \sigma^{\mu G} G \mathrm{d}^n x}{\int w\, a_{LL}\, \sigma^{\mu G} G \mathrm{d}^n x}$$

where w is a weight factor introduced in App. D. In this appendix $w = 1$.

is the ratio of longitudinally to transversally polarized virtual photon fluxes and

$$P = \frac{1}{1 + (1-y)^2} \tag{B.19}$$

is the fraction of transverse photons with spin projection antiparallel to the nucleon spin.

This leads to the following relation between muon-nucleon and photon-nucleon asymmetry:

$$\begin{aligned} A^{\mu N} &= \frac{\sigma^{\mu(\uparrow)N(\downarrow)} - \sigma^{\mu(\uparrow)N(\uparrow)}}{\sigma^{\mu(\uparrow)N(\downarrow)} + \sigma^{\mu(\uparrow)N(\uparrow)}} \\ &= \frac{(2P-1)(\sigma^T_{1/2} - \sigma^T_{3/2})}{(\sigma^T_{1/2} + \sigma^T_{3/2}) + 2\epsilon\,\sigma^L} \\ &= \frac{2P-1}{1+\epsilon R}\,A^{\gamma N} \\ &= \frac{y(2-y)}{y^2 + 2(1-y)(1+R)}\,A^{\gamma N} \\ &= D A^{\gamma N} \end{aligned} \tag{B.20}$$

where

$$R = \frac{2\sigma_L}{\sigma^T_{1/2} + \sigma^T_{3/2}} = \frac{\sigma_L}{\sigma_T}$$

is the ratio of longitudinal to transverse virtual photon absorption cross sections. Note that throughout this derivation the muon mass was neglected and we used $Q^2 \ll \nu^2$.

In eq. (B.20) the depolarization factor D has been introduced. It describes the polarization transfer from the muon to the virtual photon. In leading order QCD the Quark Parton Model expression for $A^{\gamma N}$ simply reads

$$A^{\gamma N}(x) = \frac{\sum_q e_q^2 \Delta q(x)}{\sum_q e_q^2 q(x)}\,. \tag{B.21}$$

If one analyses the muon-nucleon asymmetry in terms of various subprocesses (Leading order, QCD-Compton, photon-gluon-fusion, …) it is inconvenient to work with a photon-nucleon asymmetry. The reason is that the depolarization factor depends on the cross section ratio R which is different for different subprocesses. For the leading order process for example, we have $R = 0$ because a point-like quark cannot absorb a longitudinal photon.

With the definitions

$$\begin{aligned} \tilde{\alpha} &= a\Phi n\sigma \quad \text{and} && \text{(B.22)} \\ \beta &= P_B P_T f a_{LL} \quad \text{or} \quad P_B P_T f D && \text{(B.23)} \end{aligned}$$

eq. (B.9) reads now

$$N(\vec{x}) = \tilde{\alpha}(\vec{x})\,(1 - \beta(\vec{x})A) \tag{B.24}$$

where A stands for either $A^{\gamma N}$ or $\Delta G/G$. In eq. (B.24) the explicit dependence of α and β on kinematic variables like $Q^2, p_T, \ldots$ and other variables like the vertex position $\vec{v}$, time t, … was introduced. All these are combined in a vector $\vec{x} = (Q^2, p_T, \vec{v}, t, \ldots)$. We assume to work in kinematic bins where the physics asymmetry A ($\equiv A^{\gamma N}$ or $\Delta G/G$) does not depend on $\vec{x}$. For the inclusive asymmetry, $A^{\gamma N}$, which depends in principle on both Q^2 and x_{Bj}, the Q^2 dependence is negligible within one bin of the Bjorken variable x_{Bj}. $\Delta G/G$ is measured in a narrow momentum fraction range, where it can be assumed to be constant. Note that in principle it is possible to drop the assumption of a constant $\Delta G/G$ and allow for example for a linear dependence in the momentum fraction range considered. At the present statistical precision this seems not to be necessary.

Integration over $\mathrm{d}^n x = \mathrm{dQ^2\,dp_T d^3 v} \ldots$ leads to

$$\begin{aligned} < N >= \int N(\vec{x})\mathrm{d}^n x &= \alpha\,(1 - <\beta> A)\ , && \text{(B.25)} \\ \text{with } \alpha &:= \int \tilde{\alpha}\,\mathrm{d}^n x = \int a\Phi n\sigma\,\mathrm{d}^n x \\ \text{and } <\beta> &:= \frac{\int \tilde{\alpha}\beta \mathrm{d}^n x}{\int \tilde{\alpha}\mathrm{d}^n x}\ . && \text{(B.26)} \end{aligned}$$

Consider now two data sets, $N^{\uparrow\downarrow}$ and $N^{\uparrow\uparrow}$ with parallel and antiparallel beam and target spin. The raw counting rate asymmetry

$$A^{raw} = \frac{N^{\uparrow\downarrow} - N^{\uparrow\uparrow}}{N^{\uparrow\downarrow} + N^{\uparrow\uparrow}} \tag{B.27}$$

is related to the physics asymmetry A by

$$A^{raw} = \frac{N^{\uparrow\downarrow} - N^{\uparrow\uparrow}}{N^{\uparrow\downarrow} + N^{\uparrow\uparrow}} = \beta A = P_T P_B f a_{LL} A\ , \tag{B.28}$$

assuming

$$-\beta^{\uparrow\downarrow} = \beta^{\uparrow\uparrow} =: \beta$$

and

$$\alpha^{\uparrow\downarrow} = \alpha^{\uparrow\uparrow} \; . \tag{B.29}$$

Note that experimentally it is difficult to fulfill eq. (B.29) because it requires very good acceptance stabilization and flux normalization. For this reason the asymmetry A is extracted in a different way described in App. C. Nevertheless eq. (B.28) serves to discuss some basic aspects of the measurement of $\Delta G/G$.

Appendix C

Asymmetry Extraction

This appendix shows in detail how the asymmetry is extracted from the event yield. We start from eq. (B.24). Consider four measurements as shown in Fig. C.1. Replacing the expectation values $< N_t >$ in eq. (B.25) by the actually measured event rates N_t, $t = u, d, u', d'$ we have

$$N_t \;=\; \alpha_t \, (1- <\beta_t> A) \; . \tag{C.1}$$

Next consider the double ratio

$$\delta := \frac{N_u N_{d'}}{N_d N_{u'}} \;=\; \frac{\alpha_u \alpha_{d'}}{\alpha_{u'} \alpha_d} \; \frac{(1- <\beta_u> A)(1- <\beta_{d'}> A)}{(1- <\beta_{u'}> A)(1- <\beta_d> A)} \; . \tag{C.2}$$

Now we write for α_t :

$$\alpha_t \;=\; \{\, a_t \,\} \int \Phi_t n_t \sigma_t \mathrm{d}^n x \tag{C.3}$$

$$\text{with } \{\, a_t \,\} \;=\; \frac{\int a_t \Phi_t n_t \sigma_t \mathrm{d}^n x}{\int \Phi_t n_t \sigma_t \mathrm{d}^n x} \tag{C.4}$$

where $\{\, a_t \,\}$ is the average acceptance.

The first factor on the right hand side in eq. (C.2) can now be factorized:

$$\frac{\alpha_u \alpha_{d'}}{\alpha_{u'} \alpha_d} = \frac{\int \Phi n_u \sigma_u \mathrm{d}^n x \int \Phi' n_d \sigma_d \mathrm{d}^n x}{\int \Phi' n_u \sigma_u \mathrm{d}^n x \int \Phi n_d \sigma_d \mathrm{d}^n x} \; \frac{\{\, a_u \,\}\{\, a'_d \,\}}{\{\, a'_d \,\}\{\, a_d \,\}} \; . \tag{C.5}$$

Note that the two target cells are subject to the same flux during data taking, thus we can define $\Phi = \Phi_u = \Phi_d$ and $\Phi' = \Phi_{u'} = \Phi_{d'}$. The

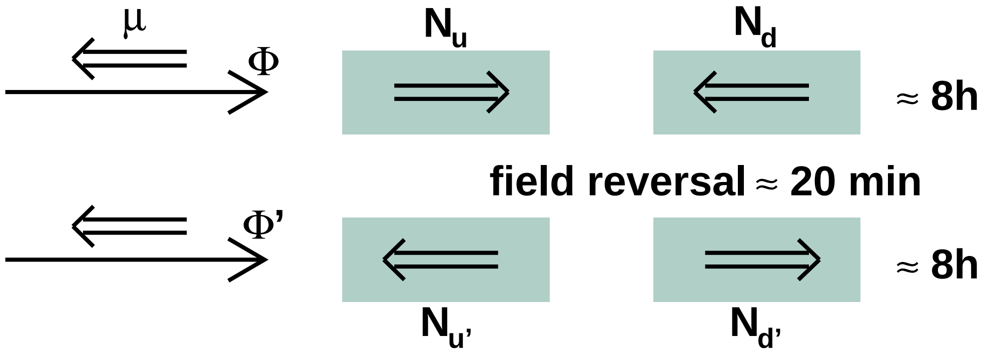

Figure C.1: To extract the asymmetry, four measurements of event rates ($N_u, N_d, N_{u'}$ and $N_{d'}$) are used. The double arrows indicate the direction of the polarization vector.

terms $\int \Phi n_t\sigma_t \mathrm{d}^n x$ can approximately be written as $\int \Phi \mathrm{d}^{\mathrm{n}_1}\mathrm{x}_1 \cdot \int \mathrm{n}_\mathrm{t}\sigma_\mathrm{t}\mathrm{d}^{\mathrm{n}_2}\mathrm{x}_2$ with $\mathrm{d}^{\mathrm{n}_1}\mathrm{x}_1 = \mathrm{d}^3\mathrm{v}\,\mathrm{dt}$ ($\mathrm{d}^3\mathrm{v}$ is the integration over the vertex position) and $\mathrm{d}^{\mathrm{n}_2}\mathrm{x}_2 =$ (all other integration variables), because Φ and Φ' depend only on the integration variables $\vec{v}$ and t whereas $n_t\sigma_t$ depends only on kinematic variables, if the target is homogeneously filled and does not move. Thus:

$$\frac{\int \Phi n_u\sigma_u \mathrm{d}^n x \int \Phi' n_d\sigma_d \mathrm{d}^n x}{\int \Phi' n_u\sigma_u \mathrm{d}^n x \int \Phi n_d\sigma_d \mathrm{d}^n x} = \frac{\int \Phi \mathrm{d}^n x_1 \int \Phi' \mathrm{d}^n x_1}{\int \Phi' \mathrm{d}^n x_1 \int \Phi \mathrm{d}^n x_1}\,\frac{\int n_u\sigma_u \mathrm{d}^n x_2 \int n_d\sigma_d \mathrm{d}^n x_2}{\int n_u\sigma_u \mathrm{d}^n x_2 \int n_d\sigma_d \mathrm{d}^n x_2} = 1\ . \tag{C.6}$$

To extract the asymmetry one has to assume that the double ratio of acceptances is 1:

$$\kappa := \frac{\{\,a_u\,\}\{\,a'_d\,\}}{\{\,a'_d\,\}\{\,a_d\,\}} = 1 \qquad \Leftrightarrow \frac{\{\,a_u\,\}}{\{\,a_d\,\}} = \frac{\{\,a_{u'}\,\}}{\{\,a_{d'}\,\}}\ . \tag{C.7}$$

In words this means that before and after a field reversal the acceptances are allowed to vary, if they vary by the same amount for the two target cells. A possible deviation of κ from 1 is a source of systematic error.

The factors $<\!\beta\!>$ can be calculated from the event sample:

$$<\!\beta\!>= \frac{\Sigma_{i=1}^{N}\beta_i}{N}\ . \tag{C.8}$$

Thus eq. (C.2) provides a quadratic equation for the asymmetry A.

The error calculation is straightforward but lengthy. For the discussion here we assume $< \beta > A \ll 1$ and $< \beta > := < \beta_u > \approx < \beta_{d'} > \approx - < \beta_{u'} > \approx - < \beta_d >$. In this case eq. (C.2) simplifies to

$$\begin{aligned} \delta &= (1 - 4 < \beta > A) && \text{(C.9)} \\ \Rightarrow A &= \frac{1 - \delta}{4 < \beta >} \; . && \text{(C.10)} \end{aligned}$$

We assume further $N_u \approx N_d \approx N_{u'} \approx N_{d'} =: N_{tot}/4$, so that

$$\sigma_\delta^2 = \frac{16}{N_{tot}} \; . \tag{C.11}$$

The figure of merit (FOM) or the statistical error on A is then given by:

$$\begin{aligned} \mathrm{FOM} = \frac{1}{\sigma_{A_S}^2} &= \left(\frac{\partial A}{\partial \delta} \right)^{-2} (\sigma_\delta)^{-2} \\ &= <\beta>^2 N_{tot} \; . && \text{(C.12)} \end{aligned}$$

Appendix D

Event Weighting

We will now consider a different way to determine the asymmetry A by giving each event a weight $w(\vec{x})$. This can provide a higher figure of merit (FOM). We start for the moment with an arbitrary weight. The observables are now

$$p_t := \Sigma_{i=1}^{N_t} w_i \quad t = u, u', d, d' \ . \tag{D.1}$$

The statistical error on $\Sigma_{i=1}^{N} w_i$ is given by $\Sigma_{i=1}^{N} w_i^2$. For $w_i \equiv 1$ this is equivalent to the asymmetry determination discussed in App C.

Multiplying eq. (B.24) with w and integrating over $\mathrm{d}^n x$ yields

$$\begin{aligned} < p > &= \int w\alpha\,(1 - \beta A)\,\mathrm{d}^n x \\ &= \int wa\Phi n\sigma \mathrm{d}^n x\,(1 - <\beta>_w A) \end{aligned} \tag{D.2}$$

where

$$<\beta>_w = \frac{\int w\alpha\beta \mathrm{d}^n x}{\int w\alpha \mathrm{d}^n x} \ . \tag{D.3}$$

This again leads to a second order equation for A:

$$\delta = \frac{p_u p_{d'}}{p_{u'} p_d} = \frac{(1 - <\beta_u>_w A)(1 - <\beta_{d'}>_w A)}{(1 - <\beta_{u'}>_w A)(1 - <\beta_d>_w A)} \ . \tag{D.4}$$

The statistical error on δ is:

$$\sigma_\delta^2 = \frac{16 \sum_{i=1}^{N_{tot}} w_i^2}{(\sum_{i=1}^{N_{tot}} w_i)^2} = \frac{16 < w^2 >}{< w >^2} \frac{1}{N_{tot}} \ ,$$

assuming

$$N_u \approx N_d \approx N_{u'} \approx N_{d'} =: \frac{N_{tot}}{4}$$

and that the average weights, $<w_t>$, are approximately the same.

The FOM is now:

$$\begin{aligned} \text{FOM} = \frac{1}{\sigma_{A_S}^2} &= \left(\frac{\partial A}{\partial \delta}\right)^{-2} (\sigma_\delta)^{-2} \\ &= <\beta>_w^2 \frac{N_{tot} <w>^2}{<w^2>} && \text{(D.5)} \\ &= \frac{<\beta w>^2}{<w>^2} \frac{<w>^2}{<w^2>} N_{tot} && \text{(D.6)} \\ &= \frac{<\beta w>^2}{<w^2>} N_{tot} \ . && \text{(D.7)} \end{aligned}$$

Up to now the weight factor w was arbitrary. Let us assume that the weight w_0 maximizes the FOM. Consider a deviation from this minimum of the form:

$$w(\vec{x}) = w_0(\vec{x}) + \epsilon\eta(\vec{x}) \tag{D.8}$$

with an arbitrary function $\eta(\vec{x})$.

The condition

$$\begin{aligned} &\frac{\partial FOM}{\partial \epsilon}|_{\epsilon=0} = \frac{\partial}{\partial \epsilon} \frac{<\beta w_0 + \epsilon\beta\eta>^2}{<(w_0 + \epsilon\eta)^2>} N_{tot} = 0 \\ &\Leftrightarrow \ < w_0\beta >< \beta\eta >< w_0^2 > - < w_0\eta >< w_0\beta >^2 = 0 && \text{(D.9)} \end{aligned}$$

is, for an arbitrary $\eta(\vec{x})$, fulfilled for $w_0 = \beta$ which means that the choice $w = \beta$ minimizes the statistical error. Applying this to eq. (D.7) results in a FOM

$$FOM = < \beta^2 > N_{tot} \ . \tag{D.10}$$

Compared to eq. (C.12) the gain in the FOM is

$$\frac{<\beta^2>}{<\beta>^2} \ . \tag{D.11}$$

Fig. D.1 shows the β distribution for the D^* event sample. The gain in the FOM is 47%. For the D^0 one reaches 40%.

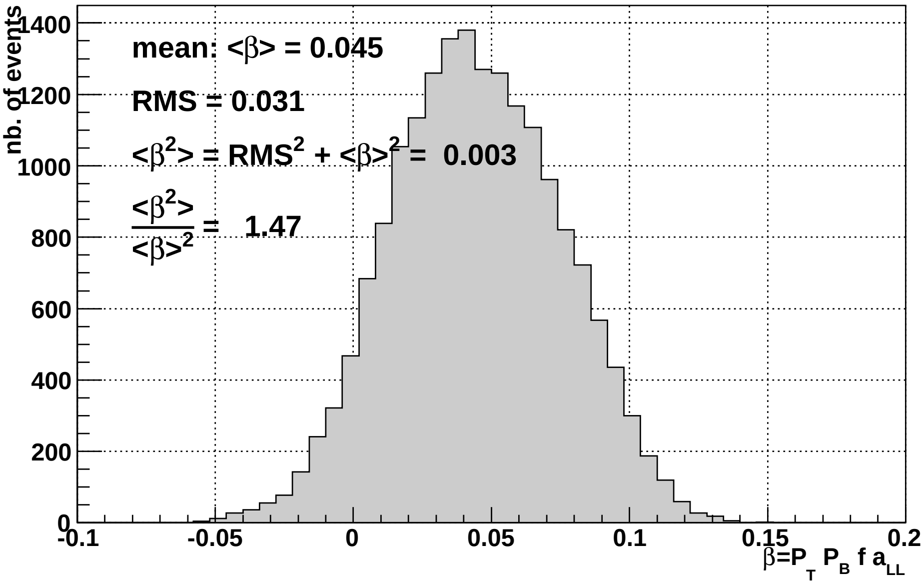

Figure D.1: The β distribution for the D^* event sample.

It is not always advisable to use the statistical optimal weight $w = \beta = P_B P_T f a_{LL}$. In the case of event weighting one has to assume

$$\kappa_w := \frac{\{\, a_u \,\}_w \{\, a_{d'} \,\}_w}{\{\, a_{u'} \,\}_w \{\, a_d \,\}_w} = 1 \tag{D.12}$$

with

$$\{\, a \,\}_w = \frac{\int a w \Phi n \sigma \mathrm{d}^n x}{\int w \Phi n \sigma \mathrm{d}^n x} \;. \tag{D.13}$$

The target polarization P_T depends on time because of repolarization or relaxation. The time dependence may even be different for the two target cells. This means that κ_w may deviate from 1 even if the acceptances are perfectly stable in time, if P_T is included in the weight. To include the target polarization P_T in the weight more care has to be taken not to introduce an additional systematic error. For this reason $w = P_B f a_{LL}$ is used. Note that the beam polarization varies event by event because of the spread of the beam momentum. It does thus make sense to include P_B in the weight.

This appendix is in large parts extracted from the COMPASS internal note[38] which contains more details.

Appendix E

Asymmetry Determination in Presence of a Polarized Background

In case of the open charm analysis eq. (B.24) has to be extended to

$$
\begin{aligned}
N &= \tilde{\alpha}\,(1 - \beta_S A_S - \beta_S A_B) && \text{(E.1)}\\
& \quad \text{with} \quad \tilde{\alpha} = a\Phi n\sigma = a\Phi n(\sigma_{PGF} + \sigma_B)\ , && \text{(E.2)}\\
& \quad \beta_S = P_B P_T f a_{LL} \frac{\sigma_{PGF}}{\sigma_{PGF} + \sigma_B}\ , && \text{(E.3)}\\
& \quad \beta_B = P_B P_T f a_{LL}^{B} \frac{\sigma_B}{\sigma_{PGF} + \sigma_B}\ . && \text{(E.4)}
\end{aligned}
$$

The reason is that the events under the mass peak of the D^0 in Figs. 6.1 and 6.2 may also carry an asymmetry A_B.

A poor man's solution would of course be to consider only events in a certain region around the mass peak (e.g. $\pm 2\sigma$), determine the asymmetry in this mass region and then determine the asymmetry of the background from the side bands in the mass spectrum and correct for it.

A better method is presented in this appendix. One has simply to consider two types of weights, one for the signal and one for the background. The corresponding weights are

$$
\begin{aligned}
w_S &= P_B f a_{LL} \frac{\sigma_{PGF}}{\sigma_{PGF} + \sigma_B}\ , && \text{(E.5)}\\
w_B &= P_B f D \frac{\sigma_B}{\sigma_{PGF} + \sigma_B}\ , && \text{(E.6)}
\end{aligned}
$$

i.e. the weights are essentially the factors β_S and β_B appearing in front of A_S and A_B in eq. (E.1) except for the target polarization P_T for the same reasons as explained in App. D. a^B_{LL} was chosen to be equal to the depolarization factor D. (A different choice would lead to a different A_B, the important fact is that A_S is not affected by the choice of a^B_{LL}). One arrives at the following 8 equations:

$$
\begin{aligned}
<\sum_{i=1}^{N_u} w_S^i> &= \alpha_{u,S}\ (1+ <\beta_{u,S}>_{w_S} A_S + <\beta_{u,B}>_{w_S} A_B) =: f_{u,S} \quad &(E.7)\\
<\sum_{i=1}^{N_d} w_S^i> &= \alpha_{d,S}\ (1+ <\beta_{d,S}>_{w_S} A_S + <\beta_{d,B}>_{w_S} A_B) =: f_{d,S} \quad &(E.8)\\
<\sum_{i=1}^{N_{u'}} w_S^i> &= \alpha_{u',S}\ (1+ <\beta_{u',S}>_{w_S} A_S + <\beta_{u',B}>_{w_S} A_B) =: f_{u',S} \quad &(E.9)\\
<\sum_{i=1}^{N_{d'}} w_S^i> &= \alpha_{d',S}\ (1+ <\beta_{d',S}>_{w_S} A_S + <\beta_{d',B}>_{w_S} A_B) =: f_{d',S} \quad &(E.10)\\
<\sum_{i=1}^{N_u} w_B^i> &= \alpha_{u,B}\ (1+ <\beta_{u,S}>_{w_B} A_S + <\beta_{u,B}>_{w_B} A_B) =: f_{u,B} \quad &(E.11)\\
<\sum_{i=1}^{N_d} w_B^i> &= \alpha_{d,B}\ (1+ <\beta_{d,S}>_{w_B} A_S + <\beta_{d,B}>_{w_B} A_B) =: f_{d,B} \quad &(E.12)\\
<\sum_{i=1}^{N_{u'}} w_B^i> &= \alpha_{u',B}\ (1+ <\beta_{u',S}>_{w_B} A_S + <\beta_{u',B}>_{w_B} A_B) =: f_{u',B} \quad &(E.13)\\
<\sum_{i=1}^{N_{d'}} w_B^i> &= \alpha_{d',B}\ (1+ <\beta_{d',S}>_{w_B} A_S + <\beta_{d',B}>_{w_B} A_B) =: f_{d',B}. \quad &(E.14)
\end{aligned}
$$

with the following definitions

$$
\begin{aligned}
\alpha_{t,C} &= \int \tilde{\alpha}_t w_C \mathrm{d}^n x \ ,\\
<\beta_{t,C}>_{w_{C'}} &= \frac{\int \beta_C w_{C'} \alpha_t \, \mathrm{d}^n x}{\int w_{C'} \alpha_t \mathrm{d}^n x} \ , \qquad (E.15)\\
& \quad t = u, d, u', d' \ , \quad C = S, B \ , \quad C' = S, B \ .
\end{aligned}
$$

As for the background free case we assume that the double ratio of acceptances equals 1. This yields the following two conditions:

$$\frac{\alpha_{u,S}\,\alpha_{d',S}}{\alpha_{u',S}\,\alpha_{d,S}} = 1 \; , \qquad \frac{\alpha_{u,B}\,\alpha_{d',B}}{\alpha_{u',B}\,\alpha_{d,B}} = 1 \; . \tag{E.16}$$

One arrives at 8 equations (E.7 - E.14) for 8 unknowns

$$A_S,\ A_B,\ \alpha_{u,S},\ \alpha_{d,S},\ \alpha_{u',S},\ \alpha_{u,B},\ \alpha_{d,B},\ \alpha_{u',B}\ .$$

In order to reduce the number of unknowns, one can try to make more assumptions. For example:

$$\frac{\alpha_{u,S}}{\alpha_{u,B}} = \frac{\alpha_{u',S}}{\alpha_{u',B}} \; . \tag{E.17}$$

This will reduce the number of unknowns from 8 to 7. The condition eq. (E.17) is even safer than the assumptions made in eq. (E.16). It only assumes that signal and background events are affected in the same way by an acceptance change before and after a field reversal. Note that eq. (E.17) implies

$$\frac{\alpha_{d,S}}{\alpha_{d,B}} = \frac{\alpha_{d',S}}{\alpha_{d',B}} \tag{E.18}$$

as well, because of eqs. (E.16).

To further reduce the number of unknowns, one can for example try to determine the ratios

$$r_u := \frac{\alpha_{u,S}}{\alpha_{u,B}} = \frac{\alpha_{u',S}}{\alpha_{u',B}} \quad \text{and} \quad r_d := \frac{\alpha_{d,S}}{\alpha_{d,B}} = \frac{\alpha_{d',S}}{\alpha_{d',B}} \tag{E.19}$$

from data. This reduces the number of unknowns from 7 to 5. Here this was done by taking

$$r_u = \frac{\sum_{i=1}^{N_u+N'_u} w_{S,i}}{\sum_{i=1}^{N_u+N'_u} w_{B,i}} \; , \tag{E.20}$$

$$r_d = \frac{\sum_{i=1}^{N_d+N'_d} w_{S,i}}{\sum_{i=1}^{N_d+N'_d} w_{B,i}} \; . \tag{E.21}$$

One value for r_u and r_d was determined per decay channel and year, thus assuming that r_u and r_d doesn't change from period to period over one year.

The reduced number of unknowns allows us to check the χ^2 as the goodness of the fit, or to introduce new unknowns, for example a background asymmetry which depends on the reconstructed mass.

The unknowns can be obtained by a χ^2 minimization:

$$\chi^2 = (\vec{N} - \vec{f})^T \, \mathrm{Cov}^{-1} (\vec{N} - \vec{f}) \, , \tag{E.22}$$

with

$$\vec{N} \;=\; \Big(\sum_{i=1}^{N_u} {w_S}^i, \sum_{i=1}^{N_d} {w_S}^i, \sum_{i=1}^{N'_u} {w_S}^i, \sum_{i=1}^{N'_d} {w_S}^i, \sum_{i=1}^{N_u} {w_B}^i, \sum_{i=1}^{N_d} {w_B}^i, \sum_{i=1}^{N'_u} {w_B}^i, \sum_{i=1}^{N'_d} {w_B}^i\Big) \, , \tag{E.23}$$

and

$$\begin{aligned} & \vec{f}(A_S, A_B, \alpha_{u,S}, \alpha_{d,S}, \alpha_{u',S}, \alpha_{u,B}, \alpha_{d,B}, \alpha_{u',B}) \\ & \quad = \; (f_{u,S}, f_{d,S}, f_{u',S} f_{d',S}, f_{u,B}, f_{d,B}, f_{u',B}, f_{d'_B}) \, . \end{aligned} \tag{E.24}$$

Since one is using the same events, once weighted with w_S and once with w_B, the 8 measurements are of course correlated. Defining $p_{t,C} = \sum_{i=1}^{N_t} w_C^i$, the covariance matrix Cov has the form shown in table E.1. The covariance between $\sum_i w_S^i$ and $\sum_j w_B^j$ is given by:

$$\begin{aligned} & \mathrm{cov}\Big(\sum_i w_S^i, \sum_j w_B^j\Big) \\ & = \; < \sum_i w_S^i \sum_j w_B^j > - < \sum_i w_S^i >< \sum_j w_B^j > \\ & = \; < \sum_{i=j} w_S^i w_B^i + \sum_{i \neq j} w_S^i w_B^j > - < \sum_i w_S^i >< \sum_j w_B^j > \\ & = \; < N >< w_S w_B > + < N(N-1) >< w_S >< w_B > - < N >^2 < w_S >< w_B > \\ & = \; < N >< w_S w_B > + (< N^2 > - < N > - < N >^2) < w_S >< w_B > \, . \end{aligned} \tag{E.25}$$

If N is Poisson distributed

$$< N^2 > - < N > - < N >^2 = \sigma_N^2 - < N > = 0$$

we are left with

$$\mathrm{cov}\Big(\sum_i w_S^i, \sum_j w_B^j\Big) \;=\; < N >< w_S w_B > \approx \sum {w_S}^i {w_B}^i \, . \tag{E.26}$$

$$\begin{pmatrix}
\delta^2 p_{u,S} & 0 & 0 & 0 & \mathrm{cov}(p_{u,S}, p_{u,B}) & 0 & 0 & 0 \\
0 & \delta^2 p_{d,S} & 0 & 0 & 0 & \mathrm{cov}(p_{d,S}, p_{d,B}) & 0 & 0 \\
0 & 0 & \delta^2 p_{u',S} & 0 & 0 & 0 & \mathrm{cov}(p_{u',S}, p_{u',B}) & 0 \\
0 & 0 & 0 & \delta^2 p_{d',S} & 0 & 0 & 0 & \mathrm{cov}(p_{d',S}, p_{d',B}) \\
\mathrm{cov}(p_{u,S}, p_{u,B}) & 0 & 0 & 0 & \delta^2 p_{u,B} & 0 & 0 & 0 \\
0 & \mathrm{cov}(p_{d,S}, p_{d,B}) & 0 & 0 & 0 & \delta^2 p_{d,B} & 0 & 0 \\
0 & 0 & \mathrm{cov}(p_{u',S}, p_{u',B}) & 0 & 0 & 0 & \delta^2 p_{u',B} & 0 \\
0 & 0 & 0 & \mathrm{cov}(p_{d',S}, p_{d',B}) & 0 & 0 & 0 & \delta^2 p_{d',B}
\end{pmatrix}$$

Table E.1: The covariance matrix for the 8 measurements.

	D^0	D^*	combined
A_S 2nd order method, ($A_B = 0$)	0.261 ± 0.700	-1.109 ± 0.547	-0.590 ± 0.431
8 parameters	0.350 ± 0.724	-1.136 ± 0.556	-0.585 ± 0.441
7 parameters	0.376 ± 0.721	-0.928 ± 0.539	-0.461 ± 0.431
5 parameters	0.313 ± 0.719	-1.075 ± 0.521	-0.597 ± 0.422

Table E.2: The results of $\Delta G/G$ for D^0 and D^* for the different methods. Only the statistical error is given.

The diagonal elements are given by

$$\delta^2 p_{t,C} \;=\; \sum_{i=1}^{N_t} (w_C^i)^2 \; , \quad t = u, d, u', d' \; , \quad C = S, B \; . \tag{E.27}$$

Results on $\Delta G/G$ are presented below

- for the normal 2nd order weighted method assuming $A_B = 0$ (App. C)
- fit method with 8 parameters
- fit method using assumption eq. (E.17) (7 parameters)
- fit method using values for r_u and r_d in eqs. (E.20,E.21) (5 parameters)

Fig. E.1 and Tab. E.2 show the results for D^0 and D^* for the different methods. The results differ only by a small fraction of the statistical error. Fig. E.2 shows the χ^2 probability distribution for the fit with 7 and 5 parameters. There is one entry per period and decay channel (D^0 or D^*). They are not incompatible with the expected flat distribution.

As can be seen in Tab. E.2 the fit with 5 parameters leads to the smallest statistical error. But here the required values for r_u and r_d are taken from the same events which are used later to extract the asymmetry. Taking values for $r_{u,d}$ period per period, instead of the values for the whole year, results in a χ^2 probability distribution with abnormal high values for the probabilities. This is clear since one uses exactly the same data to determine $r_{u,d}$ as used in the fit. If one takes one value per year this effect gets diluted. In the final result the method with 7 parameters is retained.

Up to now the full mass spectrum in the range ±400 MeV was used in the fits. Figs. E.3 and E.4 show the result on $\Delta G/G$ and A_B for different

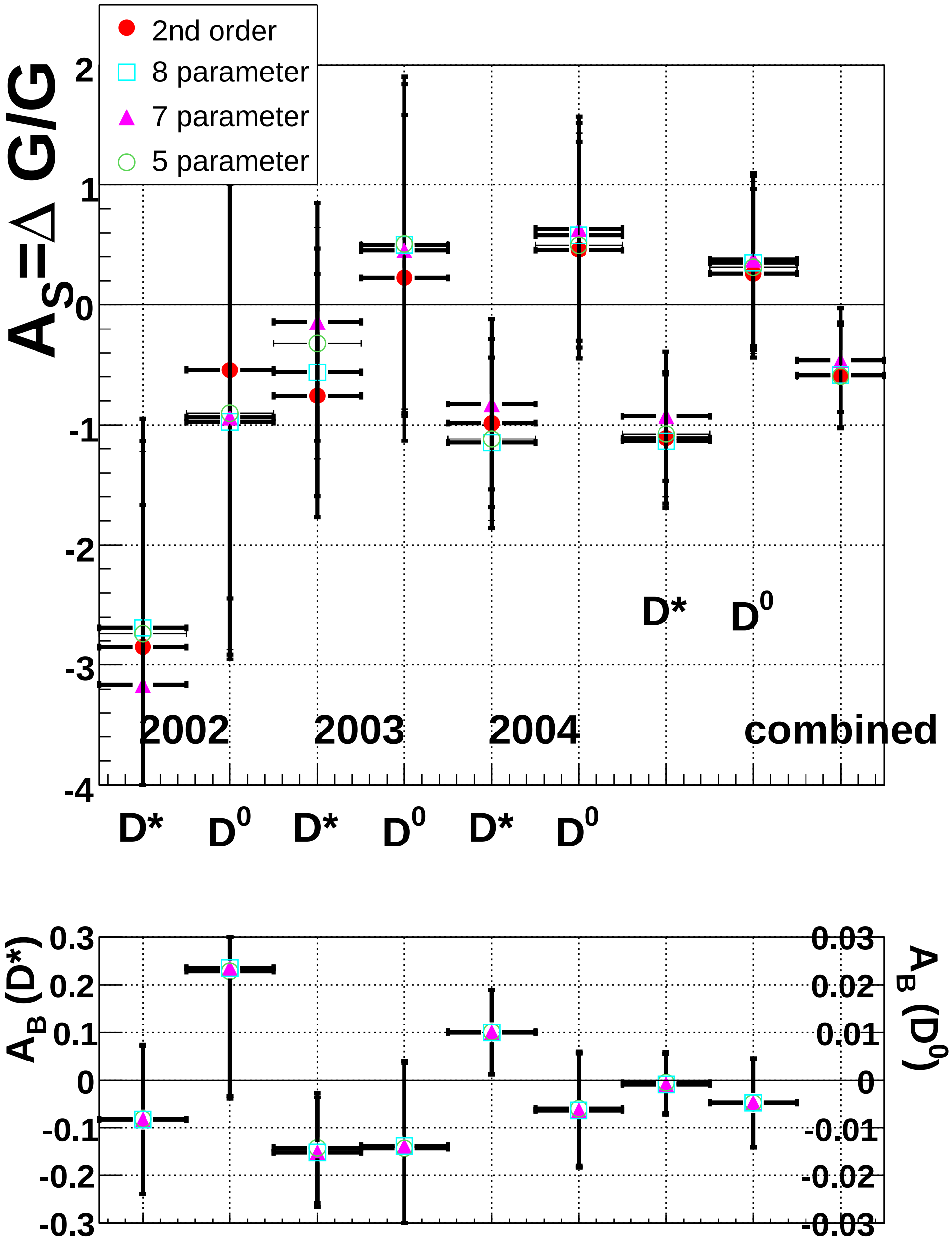

Figure E.1: The upper plot shows the results on $\Delta G/G$ for D^* and D^0 for different years and different methods (2nd order, 8,7, and 5 parameter fits). The lower plot shows the corresponding background asymmetries. The horizontal axis is the same for both histograms. Note that in the lower histogram the left vertical scale is for the D^* background asymmetry and the right scale for the D^0 background asymmetry.

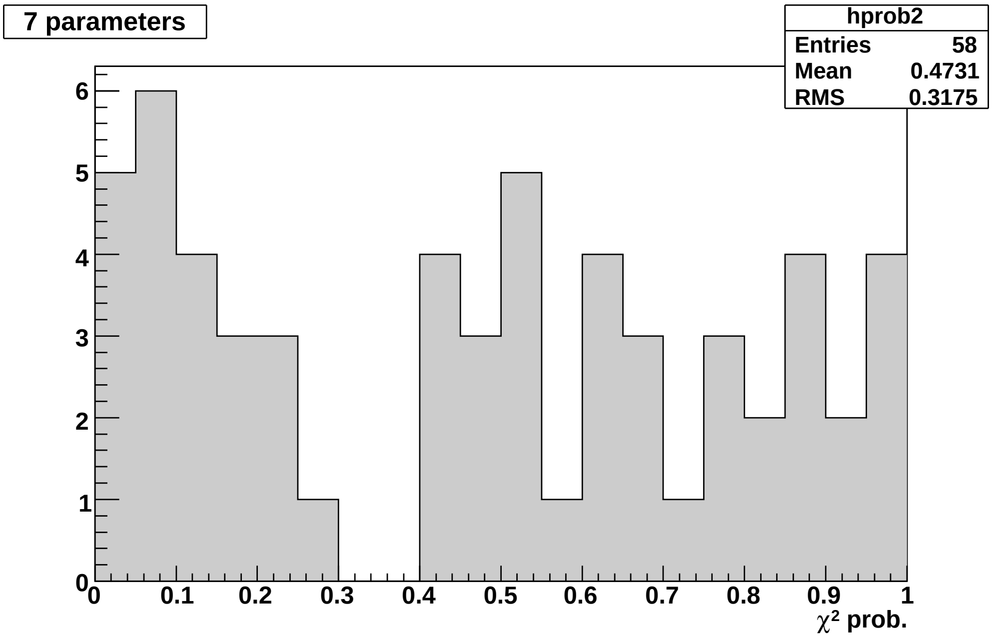

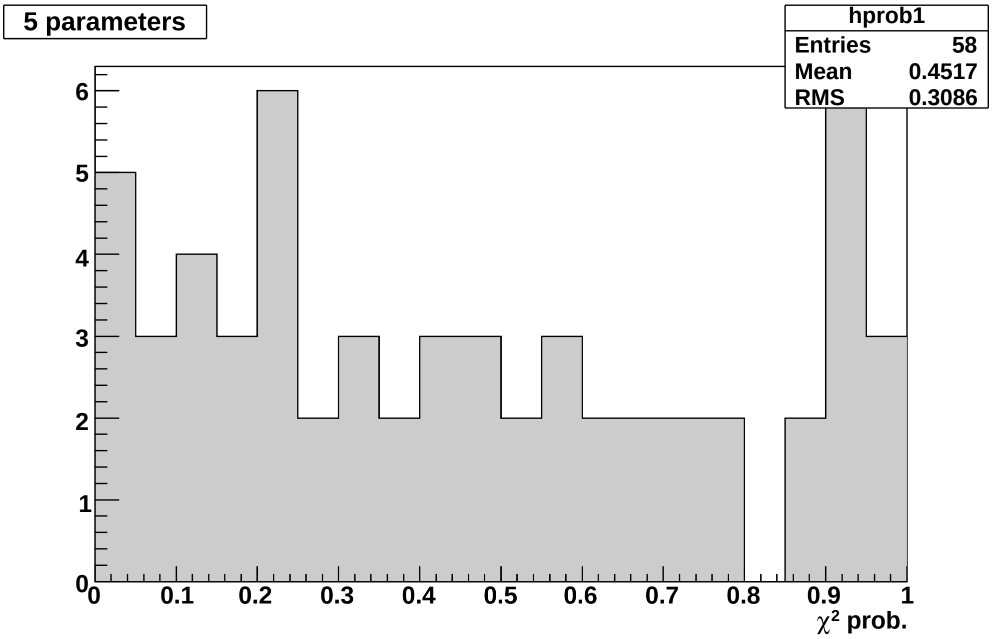

Figure E.2: The χ^2 probability distribution for the fit with 7 and 5 parameters. There is one entry per period and decay channel (D^0 or D^*).

mass ranges down to ±50 MeV for the D^0 and the D^*. The lines show the expected 1 σ deviations from the point with the smallest statistical error at 400 MeV which was used in the analysis. No peculiar behavior is observed in these plots.

This appendix is based on a COMPASS internal note[39] which contains more details.

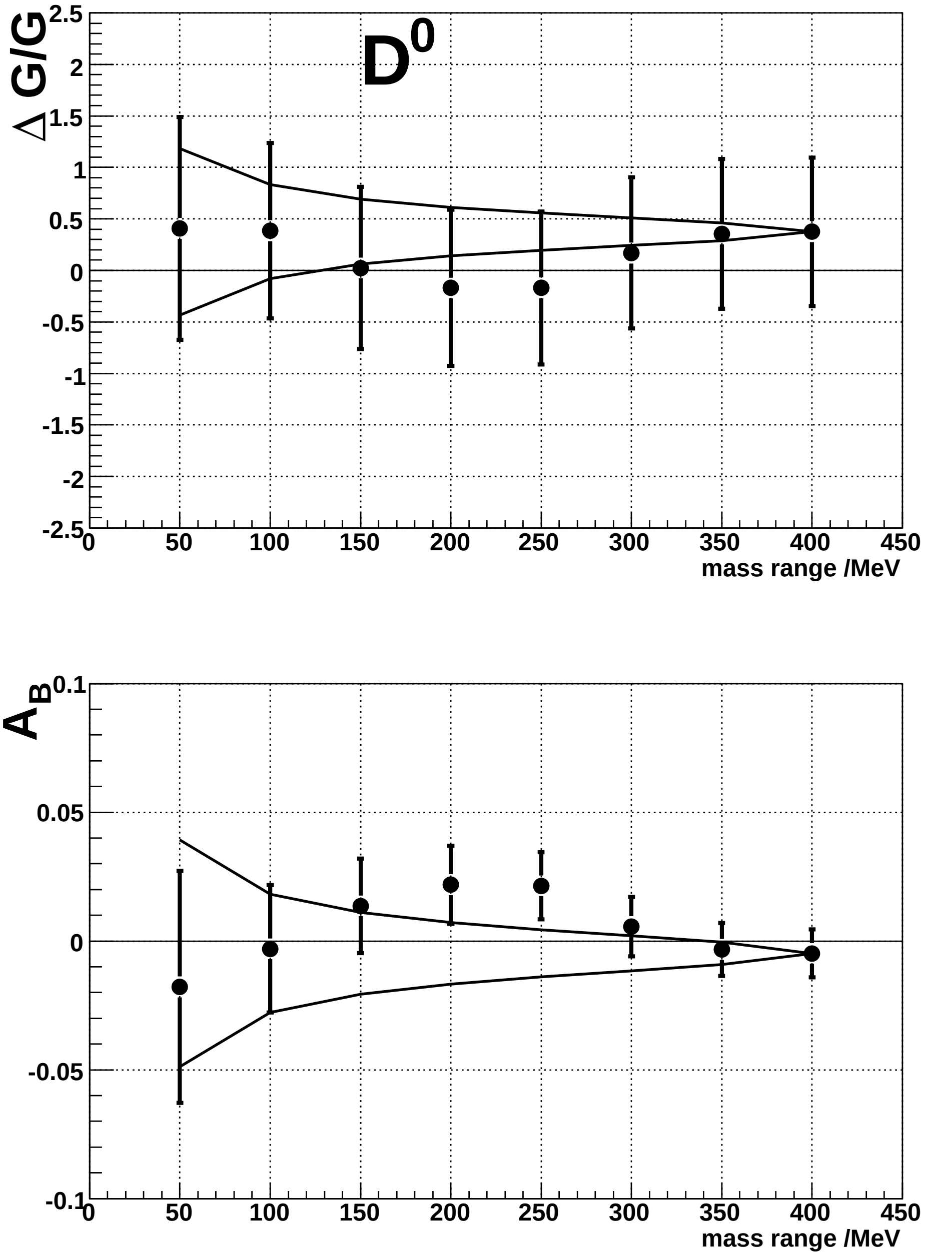

Figure E.3: Dependence of $\Delta G/G$ and A_B on the mass range of the 7 parameter fit for D^0. The lines in the plots show the expected 1 σ deviations from the point with the smallest statistical error at 400 MeV.

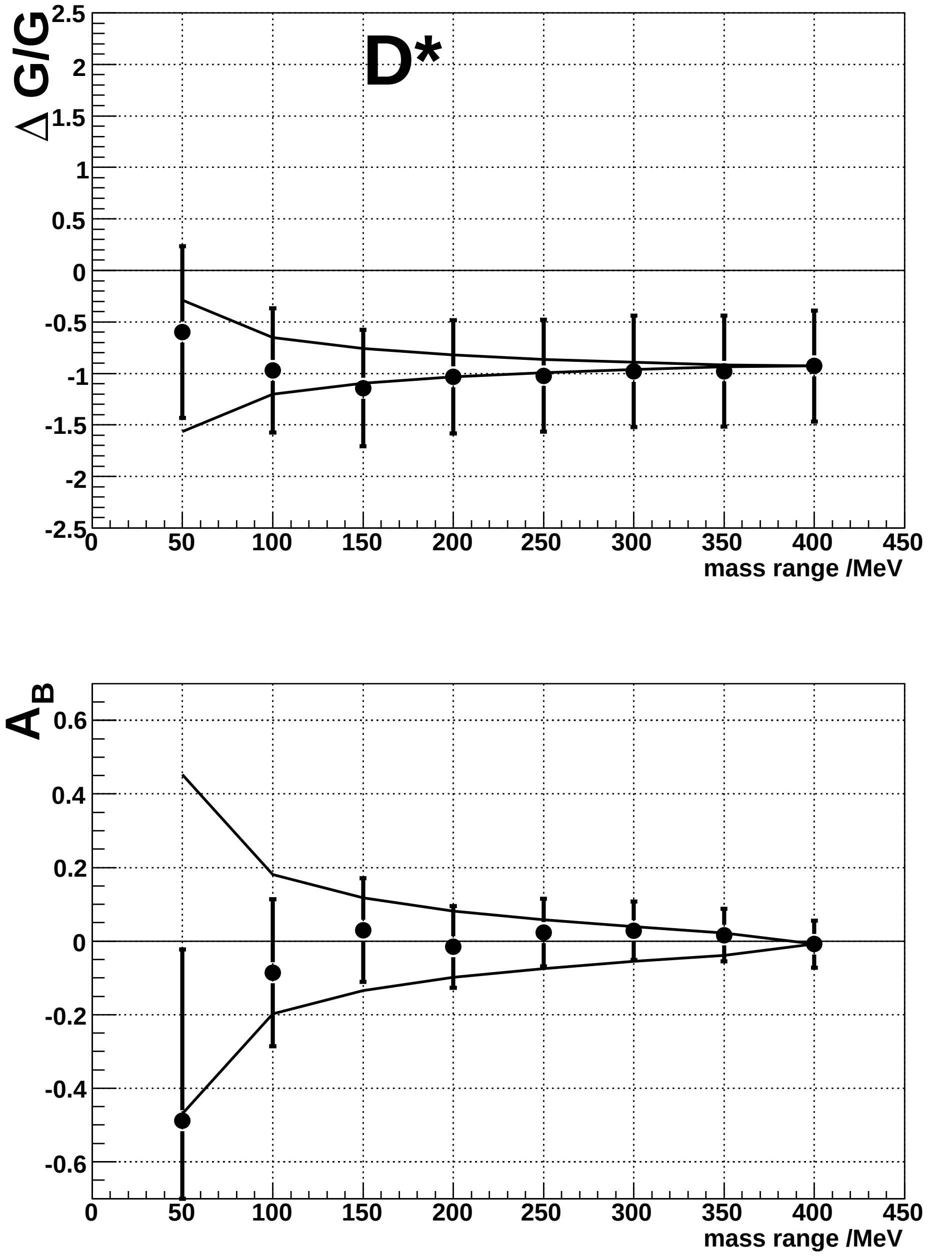

Figure E.4: Dependence of $\Delta G/G$ and A_B on the mass range of the 7 parameter fit for D^*. The lines in the plots show the expected 1 σ deviations from the point with the smallest statistical error at 400 MeV.

Bibliography

[1] E. Leader, E. Predazzi
An Introduction to Gauge Theories and Modern Particle Physics, Vol. 1 & 2
Cambridge University Press, 1996

[2] E. Leader
Spin in Particle Physics
Cambridge University Press, 2001

[3] J. Levelt, Thesis,
Deep inelastic semi-inclusive processes,
Amsterdam, 1993

[4] F. Close,
An Introduction to Quarks and Partons ,
Academic Press Inc., 1979

[5] J. F. Cornwell,
Group Theory in Physics,
Academic Press, London, 1984

[6] R. D. Carlitz, J. C. Collins and A. H. Mueller,
Phys. Lett. B **214** (1988) 229

[7] M. J. Alguard *et al.*,
Phys. Rev. Lett. **37** (1976) 1261

[8] J. Ashman *et al.* [European Muon Collaboration],
Phys. Lett. B **206** (1988) 364

[9] J. Ashman *et al.* [European Muon Collaboration],
Nucl. Phys. B **328** (1989) 1

[10] G. Preparata, J. Soffer,
Phys. Rev. Lett. **61**, 1167 - 1169 (1988)

[11] E. Leader, A. V. Sidorov and D. B. Stamenov,
Phys. Rev. D **73** (2006) 034023

[12] V. Y. Alexakhin *et al.* [COMPASS Collaboration],
arXiv:hep-ex/0609038

[13] A. Bravar, D. von Harrach and A. Kotzinian,
Phys. Lett. B **421** (1998) 349

[14] A. Bravar, K. Kurek and R. Windmolders,
Comput. Phys. Commun. **105** (1997) 42

[15] COMPASS Proposal
CERN SPSLC 96-14

[16] R. Machleidt, K. Holinde and C. Elster,
Phys. Rept. **149** (1987) 1

[17] P. Abbon *et al.*
hep-ex/0703049
acc. for publication in Nucl. Instrum. Meth. A

[18] C. Bernet *et al.*,
Nucl. Instrum. Meth. A **550** (2005) 217

[19] M. v. Hodenberg, Dissertation, Freiburg, 2005

[20] S. Koblitz, Dissertation, Mainz, 2007, in preparation

[21] G. Ingelman, J. Rathsman and G. A. Schuler,
Comput. Phys. Commun. **101** (1997) 135

[22] J.-M. Le Goff , COMPASS internal note 2004-3

[23] PYHTIA
T. Sjostrand, S. Mrenna and P. Skands,
JHEP **0605** (2006) 026

[24] LEPTO
G. Ingelman, A. Edin and J. Rathsman,
Comput. Phys. Commun. **101** (1997) 108

[25] B. Adeva *et al.* [Spin Muon Collaboration (SMC)],
Phys. Rev. D **70**, 012002 (2004)

[26] E. S. Ageev *et al.* [COMPASS Collaboration],
Phys. Lett. B **633** (2006) 25

[27] M. Glück, E. Reya and C. Sieg,
Eur. Phys. J. C **20** (2001) 271

[28] S. Procureur, Thèse, Université Paris XI, 2006

[29] S. Hedicke, Dissertation, Freiburg, 2005

[30] M. Glück, E. Reya, M. Stratmann and W. Vogelsang,
Phys. Rev. D **63**, 094005 (2001)

[31] B. I. Abelev *et al.* [STAR Collaboration],
Phys. Rev. Lett. **97** (2006) 252001

[32] K. Boyle [PHENIX Collaboration],
hep-ex/0701048

[33] G. K. Mallot,
hep-ex/0612055

[34] A. Airapetian *et al.* [HERMES Collaboration],
Phys. Rev. Lett. **84** (2000) 2584

[35] P. Liebing [HERMES Collaboration],
Proceedings 17th International Spin Physics Symposium (SPIN 2006),
Kyoto, Japan, 2006

[36] A. Deshpande, *et al.*
Ann. Rev. Nucl. Part. Sci. **55** (2005) 165

[37] X. D. Ji,
Phys. Rev. Lett. **78** (1997) 610

[38] J. Pretz, COMPASS internal note 2004-11

[39] J. Pretz, COMPASS internal note 2005-12

Acknowledgment, Danksagung, Remerciements

An dieser Stelle ist es Zeit allen denjenigen Dank zu sagen, die zum Gelingen dieser Arbeit beigetragen haben.

- Mein erster Dank geht an Prof. Klein, der mir ermöglicht hat diese Habilitationsschfrift anzufertigen.
- Desweiteren möchte ich mich bedanken bei den Mitgliedern unserer Arbeitsgruppe und der Arbeitsgruppe von Prof. v. Harrach in Mainz: J. Barth, J. Hannappel, R. Hermann, E. Kabuß, A. Korzenev, S. Koblitz, M. Leberig M. Ostrick, R. Panknin und J. Zhao für die angenehme Zusammenarbeit beim Aufbau und Betrieb des Triggersystems und der Analyse der Daten
- Un grand merci a Jean-Marc Le Goff et Roland Windmolders, non seulement pour lire le manuscrit, mais aussi pour des innombrables discussions concernant la physique de SMC et COMPASS.
- This work would not have been possible without the effort of many people in the COMPASS collaboration, impossible to name all of them. Ich möchte hier nur Gerhard Mallot nennen, mit dem ich schon zu Zeiten des SMC Experimentes eng zusammengearbeitet habe.
- Ein letztes Dankeschön geht an meine Frau Anke und unsere Kinder Corinne und Pascal, die immer für den nötigen Ausgleich gesorgt haben.